

LAPPEENRANTA UNIVERSITY OF TECHNOLOGY

School of Engineering Science

Technical Physics

*Elizaveta Filippova*

**ATOMIC FORCE MICROSCOPY (AFM) MEASUREMENTS OF COMPOSITE  
MEMBRANES BASED ON CHITOSAN AND DEEP EUTECTIC SOLVENT**

Examiners: Professor Erkki Lähderanta  
Kand. Nauk Mikhail Smirnov

## **ABSTRACT**

LAPPEENRANTA UNIVERSITY OF TECHNOLOGY

School of Engineering Science

Technical Physics

Elizaveta Filippova

### **Atomic force microscopy (AFM) measurements of composite membranes based on chitosan and deep eutectic solvent**

Master's thesis

2017

60 pages, 23 figures and 5 tables

Examiners: Professor Erkki Lähderanta  
Kand. Nauk Mikhail Smirnov

Keywords: chitosan, deep eutectic solvent, atomic force microscopy, PeakForce QNM, PeakForce TUNA

The composite membranes based on chitosan and deep eutectic solvent (DES), namely eutectic mixture of choline chloride and malonic acid, were prepared and studied by means of atomic force microscopy. PeakForce QNM and PeakForce TUNA modes permitted to visualize surface topography simultaneously with mapping of mechanical and electrical properties.

Surface heterogeneity was shown for the films with high DES content. The obtained Young's modulus values were in qualitative agreement with bulk measurements by uniaxial extension. The topography and adhesion of films with high DES content were found to depend on the bias applied to the film.

## **ACKNOWLEDGEMENTS**

It is my pleasure to thank all the people who helped me on my way to completing Master's Thesis.

First of all, I would like to thank Erkki Lähderanta for providing me with an opportunity to study at Lappeenranta University of Technology and to participate in an interesting and relevant research. I am also deeply grateful to my supervisor Mikhail Smirnov for his guidance, advice and help during my work on the Master's Thesis.

I would also like to acknowledge a gratitude to Pavel Geydt for his mentorship in atomic force microscopy and fruitful discussions. I am thankful as well to Ekaterina Soboleva and Maria Sokolova for their assistance.

Last but not least, I extend my thanks to my friends and family for their support and to everyone I met during my studies in Lappeenranta for making this year unforgettable.

Lappeenranta, May 2017

Elizaveta Filippova

## **Table of contents**

<b>1. Introduction</b>	6
<b>2. Theoretical part</b>	8
2.1. Chitosan	8
2.1.1. Chitin and chitosan properties	8
2.1.2. Chitosan applications	10
2.2. Ionic liquids	14
2.2.1. “Common” ionic liquids	14
2.2.2. Deep eutectic solvents	15
2.3. Polymer/IL and polymer/DES composites	18
<b>3. Objectives of this work</b>	22
<b>4. Methodical part</b>	23
4.1. Scanning probe microscopy: Basic principles	23
4.2. Atomic Force Microscopy	23
4.3. PeakForce QNM <sup>®</sup> mode	28
4.4. PeakForce TUNA <sup>®</sup> mode	31
<b>5. Experimental</b>	35
5.1. Samples preparation	35
5.2. Measurements	35
<b>6. Results</b>	38
6.1. Topography	38
6.2. Mechanical properties	41
6.3. Electrical properties	44
<b>Conclusions</b>	51
<b>Summary</b>	52
<b>References</b>	54

## List of abbreviations and symbols

AFM	atomic force microscopy; atomic force microscope (device)
DES	deep eutectic solvent
DMT	Derjaguin–Muller–Toporov (model)
HBD	hydrogen bond donor
IL	ionic liquid
QNM	quantitative nanomechanical properties mapping
SPM	scanning probe microscopy
TUNA	tunneling AFM
$d-d_0$	deformation of the sample
$E$	Young's modulus
$E^*$	reduced Young's modulus
$F-F_{adh}$	the force on the cantilever relative to the adhesion force
$k$	cantilever's spring constant
$R$	resistance
$r$	tip radius
$T_g$	glass transition temperature
$w$	cantilever's resonance frequency
$\Delta Z$	displacement of the tip height

## 1. Introduction

With growing environmental concern, “green” materials are nowadays of great interest in different areas of industry and research. Natural polymers and their derivatives hold a special place among environmentally friendly materials.

Recently, much attention has been given to chitin, which is the second most abundant natural polymer after cellulose, and to its derivative chitosan [1–3]. Chitin, chitosan and their derivatives are promising materials for industrial and medical applications. These polymers are attractive due to their biocompatibility and biodegradability as well as immunomodulating, antimicrobial, fungistatic, antitumoral, radioprotective, anti-inflammatory, anticholesteric and hemostatic properties. In addition, unlike most natural polymers, chitin and chitosan are positively charged, which plays a significant role in their application. While chitin is insoluble in water, diluted acids, alkalies, alcohols and other organic solvents, chitosan dissolves even in diluted organic acids, e.g., in water solution of acetic acid, which facilitates its usage.

Polymer properties can be significantly improved by adding modifiers to the materials. A large group of compounds that may be used for this purpose is represented by ionic liquids. Ionic liquid (IL) is an organic salt consisting entirely of ions and with melting point lower than 100 °C [4, 5]. The areas of IL application include metal processing, biodiesel synthesis, gas and azeotropic mixtures separation, pervaporation, catalysis, fabrication of “artificial muscles”, usage as reaction media and electrolytes for fuel cells [6–11]. Composites of polymers with ILs are used for gas separation [11–15], pervaporation [16, 17] and for fabrication of “artificial muscles” [10, 18–20].

However, the application of ionic liquids is shown to be potentially hazardous to the environment [5, 21]. Thus, alternative modifiers for polymers are needed, which would have lower environmental impact while being able to perform the same functions as ILs. Such a “greener” analog of ILs has been found in the form of deep eutectic solvents [22, 23].

Deep eutectic solvent (DES) is a eutectic mixture formed when two or three components associate with each other via hydrogen bond interactions; a melting point of the resulting DES is much lower than that of each individual component [24]. DESs of the most adaptable and the most widely used type consist of choline chloride and hydrogen bond

donors, which may be urea, carboxylic acids or polyols [24, 25]. Choline chloride usage is favorable due to its low cost, low toxicity, biodegradability and almost waste-free production.

A number of applications of choline-based DESs for polymer modification have been reported [26–31]. However, the composites of DESs with chitosan are almost unexplored; to the best of our knowledge, only one study addresses this issue [31].

Therefore, the **motivation** of this work was to prepare composite films of chitosan and DES and to determine their surface topography as well as mechanical and electrical characteristics. A eutectic mixture of choline chloride and malonic acid was used as a DES.

The literature survey shows successful application of atomic force microscopy for polymer surface study [32–35]. The up-to-date atomic force microscopy techniques allow simultaneous measurements of topography, mechanical properties and current through the sample [36, 37] Therefore, atomic force microscopy was chosen as an experimental technique in this work.

This work is **structured** as follows:

- Theoretical part reviews properties and applications of chitin and chitosan as well as of ionic liquids and deep eutectic solvents, paying special attention to composites of polymers with ILs and DESs;
- this part is followed by Objectives of this work;
- Methodical part describes the operational principles of atomic force microscopy and the modes used in this work;
- Experimental part describes the sample preparation and the sequence of measurements;
- Results present the discussion of the measurements results;
- in Conclusions, the observations and obtained results are analyzed;
- Summary concisely describes this work, giving also the ideas for the future.

## 2. Theoretical part

### 2.1. Chitosan

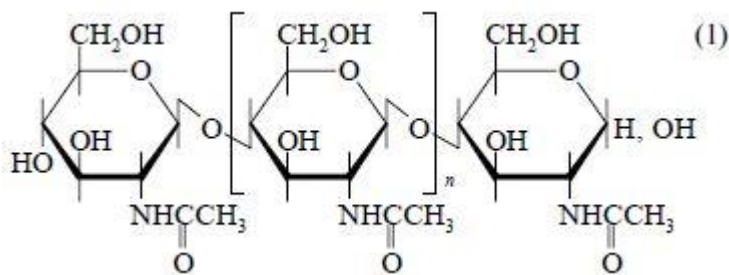
#### 2.1.1. Chitin and chitosan properties

Natural polymer chitin and its derivative chitosan are attractive due to their biocompatibility and biodegradability as well as immunomodulating, antimicrobial, fungistatic, antitumoral, radioprotective, anti-inflammatory, anticholesteric and hemostatic properties. Chitin, chitosan and their derivatives are promising materials for industrial and medical applications.

Chitin is the second most abundant natural polymer after cellulose. Chitin is a white, hard, inelastic polysaccharide, which is a component of the exoskeletons and internal structures of crustaceans and insects; fungi and some algae also contain chitin.

Alongside with chitin, crustacean and insect shells contain proteins and calcium carbonate, so obtainment of a pure chitin requires for deproteinization and demineralization [1, 38].

Chitin macromolecule consists of a linear chain of  $\beta$ -(1 $\rightarrow$ 4)-linked 2-acetylamino-2-desoxy-D-glucose (N-acetyl-D-glucosamine) units:



Thus, chitin macromolecule structure is similar to that of cellulose, but with one hydroxyl group of each monomeric unit replaced with an acetyl amide group. Natural chitin usually contains a small number of free amines.

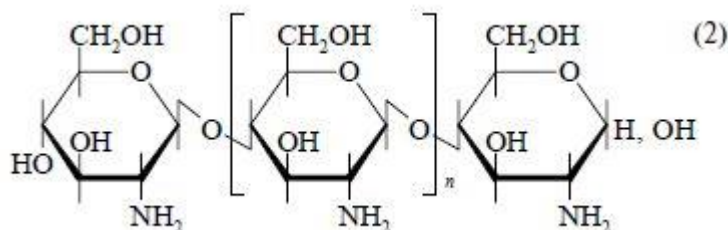
Chitin macromolecules aggregate to form microfibrils 2.5 – 2.8 nm in diameter, which in turn form fibrils 25 – 50 nm in diameter. This supramolecular structure increases mechanical strength of chitin containing tissues.

Chitin has a highly-ordered crystalline structure due to its tacticity. There are three crystallographic modifications of chitin with molecular chains differently arranged within

the lattice cell (this phenomenon being called polymorphism).  $\alpha$ -chitin, which is the most abundant modification, has tightly packed antiparallel macromolecules.  $\beta$ -chitin having parallel chains exists as relatively stable crystalline hydrates. Unit cell of  $\gamma$ -chitin contains two parallel chains and one antiparallel to them.

Although chitin cannot be fully crystalline, it contains about 60 – 85% crystalline areas depending on the origin and extraction method.

The most interesting chitin derivative, chitosan, which is obtained via chitin deacetylation, has monomeric units of  $\beta$ -(1 $\rightarrow$ 4)-linked 2-amino-2-desoxy-D-glucose (D-glucosamine):



Even after deacetylation in rigid conditions, chitosan contains some N-acetyl-D-glucosamine units, because acetyl amine groups are highly hydrolytic stable.

Like chitin, chitosan is an amorphocrystalline polymer, which also possesses polymorphism, number of structural modifications increasing to 6. The unit cell size along the macromolecular axis remains the same (103 nm), which indicates the absence of significant conformational changes during chitin to chitosan transition. However, the crystallinity degree decreases to 40 – 50%, which can result both from intracrystalline swelling and from irregularity in the case of some N-acetyl groups remaining.

While most natural polysaccharides are electrostatically neutral or possess a negative charge, chitin and chitosan are cationic polysaccharides. Electrostatic interactions of chitosan with anionic compounds are important for its applications [2].

Chitin is a hydrophobic compound, which is insoluble in water, diluted acids, alkalis, alcohols and other organic solvents. It is soluble in strong solutions of mineral acids (hydrochloric, sulfuric, nitric, phosphoric) and anhydrous formic acid, as well as in hexafluoroisopropanol, hexafluoroacetone, chloroalcohols and dimethyl acetamide containing 5% lithium chloride. However, dissolution in most of these solvents is accompanied by noticeable chitin depolymerization [1, 2].

Polymer destruction during dissolving hinders determination of molecular weight true value and of molecular mass distribution. For instance, chitin extracted from crustacean shells has a molecular mass equal to  $2\text{--}2.5 \cdot 10^6$  Daltons and degree of polymerization equal to 10,000–14,000 [1].

Unlike chitin, chitosan dissolves even in diluted organic acids, e.g., in water solution of acetic acid [1]. Chitosan possesses significant viscosity temperature dependence, which is a feature of all polymers. A free amine in each monomeric unit makes chitosan polyelectrolytic, which includes polyelectrolytic swelling, i.e. anomalous viscosity increase of diluted solutions (concentration less than 1 g/l) with polymer concentration decrease. This effect results from the effective volume increase due to the repulsion of similar charges generated when amines are protonated.

Depending on the origin and extraction method, chitosan molecular weight equals to  $0.5\text{--}8 \cdot 10^5$  Daltons. Significant difference between chitin molecular weight and that of chitosan indicates noticeable polymer chain destruction during deacetylation [1].

Chitin and chitosan chemical transformations are of great concern as these polysaccharides are close to cellulose by their functional composition, which makes it possible to obtain derivatives analogous to existing cellulose derivatives. These include ethers (methyl, ethyl, carboxymethyl, hydroxyethyl) and esters of inorganic (nitrates, sulfates, xanthogenates) and organic (acetates) acids. Free amines present in a chitosan molecules and possibility to protect them under reaction conditions allows synthesis of selectively substituted derivatives. Hybrid copolymers combining natural and synthetic polymer properties can also be synthesized, as well as branched polysaccharides of complex structure [1, 39].

### 2.1.2. Chitosan applications

Due to its physical and chemical properties, chitosan can be used in different areas ranging from pharmaceuticals and cosmetics to water treatment and textile industry.

#### *Industrial applications*

As chitin and chitosan molecules are similar to those of cellulose, they are utilized in paper industry. When cellulose fibers are coated with chitosan, the paper sheet becomes stronger, especially in the wet state. Burst strength, folding endurance and image stability also

improve. In addition, chitosan is used for toilet paper, folding paper, cardboard and food wrap production [1, 2].

Another area of chitin and chitosan application is textile industry. Chitin derivatives give antistatic and dirt-resistant properties to the fabric. Production of textiles for medical applications, e.g. retention sutures, also utilizes chitin and chitosan [2].

As a chelating agent, chitosan can be used for water treatment, i.e. extracting of heavy metals, radionuclides, bacteria, many organic impurities, oil products, pesticides and other compounds. Chitin and chitosan are also promising for hydrometallurgical processes of metals of value extraction from industrial waste liquids or from sea water [2, 3, 40].

Horticulture utilizes chitin and its oligomers as well as chitosan primarily for crops protection against phytopathogenic microorganisms influence. Chitin both improves plants resistivity to pathogens and inhibits fungi growth; amount and species composition of pathogenic microorganisms and nematodes decreases in soil containing chitin. As a result, output yield increases. However, high chitin content can lower crops fertility, e.g. that of crops, which is likely due to chitin's ability to suppress nitrogen-fixing bacteria [3].

Food industry also widely uses chitosan, as it is non-toxic for human and warm-blooded animals. For instance, chitosan is a convenient sorbent for nutrients extraction from sera and rinsates. In addition, chitosan is used for water purification and clarification of different drinks including alcoholic ones. Lipid peroxidates, which deteriorate foods marketability and edibility, can also be removed from foods through the use of chitosan. Chitosan's ability to form gels of different consistence allows for foods thickening, gelation and densifying, as well as development of novel thermostable biologically active gelling additives of low energy value. Chitosan and its derivatives can also act as natural preservatives which protect vegetables, fruits and berries against rotting [3, 41].

Cosmetics utilizes chitin, chitosan and their derivatives for hair care, skin care and oral care. Positively charged chitosan is capable of interactions with negatively charged biological tissues — hair and skin. Chitosan-containing shampoos are antistatic; they improve hair elasticity and act against scruffs. Due to its gel-forming ability, chitosan can be used as natural compound for hairdressing and waving. Antibacterial properties and hypoallergenicity of chitosan make it a possible component of creams for problem skin.

Alongside with different fillers, chitosan can be used in anti-cavity toothpastes, which can reduce adhesive properties of plaque bacteria [2, 3, 42].

Chitin and chitosan are widely used in chromatographic separation. Free amines, primary and secondary hydroxyls make chitosan a suitable chromatographic substrate. Nucleic acids separation by using chitosan is reported [2, 43].

Chitosan is also used in color photography; it is a promising compound for secondary solid-state cells and light-emitting devices [2].

Recently chitosan has been shown to be a promising material for biological functionalization of microelectromechanical systems (bioMEMS). Due to the unique chemical properties and film-forming ability, chitosan can act as a matrix for assembly of biomolecules, cells, nanoparticles, etc. Addition of these components to bioMEMS-devices enables functions such as specific biorecognition, enzymatic catalysis and controlled drug release [44].

#### *Application for biotechnology and medicine*

Chitin, chitosan and their derivatives are of special interest for medical industry as they are biocompatible, biodegradable, low-toxic and capable of intensifying regeneration in the process of wound healing. Chitosan is not only a bioactive compound, but also a promising substance for bioencapsulation [45]. Bioencapsulation implies creation of polymer systems with immobilized biomaterial, which can be both various bioactive substances (proteins, including enzymes, DNA, peptides, low-molecular hormones, antibiotics, etc.) and living cells.

Chitosan and its derivatives can be used for detoxification in cases of digestive system inflammatory diseases, as it possesses enterosorbent and immunomodulating properties and inhibits growth of some microorganisms. These diseases include general peritonitis, pancreatitis and acute kidney injury [46].

For blood-clotting treatment and prevention medicine uses heparin, natural anticoagulant polysaccharide that has a structure similar to that of a chitosan sulfate. Chitosan sulfate possesses anticoagulant properties and can enhance anticoagulant and antisclerotic action of heparin [47].

Chitosan can form stable complexes with lipids, which motivates its application as food supplement for weight reduction, lowering risks of cardiovascular diseases, rectal cancer and cholecystitis [3].

Sulfated chitosan derivatives are reported to be promising for HIV treatment as they are able to disturb adsorption processes crucial for HIV progression and hinder avalanche agglutination of infected cells with intact ones [48].

Chitin, chitosan and their derivatives can be used also in cancer therapy, as they selectively center around cancer cells, inhibiting their growth [3, 48].

Chitosan and its derivatives are successfully implemented for wound and burn healing polymer coatings. As all such coatings, chitosan-based ones are nontraumatic and highly sealing; they provide wound drainage, protection against external infection and possibility to intensify healing process, as these coatings are suitable substrates for cells migration, adhesion and proliferation. In addition, chitosan coatings possess several specific properties. Chitosan stimulates macrophagocytes and enhances fibroblast proliferation, while acetyl glucosamine can be used to produce mucopolysaccharides, which intensifies wound healing. Although chitosan itself positively affects the healing process, the highest effect can be achieved by encapsulating drugs into the coatings. These drugs include anesthetic, antibacterial and hemostatic medications, antioxidants, growth factors and proteolytic enzymes [45, 49].

Chitosan is a basis of a wide range of polymer systems for drug delivery and prolonged release through mucous membranes, particularly when used orally. These systems should deliver drugs precisely to the diseased organ and release it when needed and in minimal amount, which significantly reduces drug dosage and prevents side effects. They should also protect bioactive compound from proteolytic enzymes and gastric acid media and enable penetrating through intestinal walls. Chitosan has been proposed for oral delivery of cancer and colitis treatment drugs and of insulin, as well as for intranasal drug delivery [45, 48, 49]. Chitosan and its derivatives can be used also for oral and nasal prolonged vaccines, which are released during 1 – 6 months, thus not requiring for hypervaccination [45].

Chitosan can also be a basis of injectable gels, i.e. polymer water solutions that are injected intramuscularly and form a gel inside the human body [1, 3, 45, 48]. These gels, which are used particularly for reconstructive surgery of bones and cartilaginous tissues, take the

shape of a defect and can contain growth factors and other therapeutic agents, and their injection does not require a surgical operation. Intramuscular injection of drug-containing microcapsules is also possible.

Chitosan is a promising material for genetic engineering, as it can associate with DNA and deliver it into the cell [45, 50]. This can be also implemented for genetic therapy.

Genetically engineered animal cells can also be placed into a microcapsule and then implanted into a human body, being protected from host immune system and having ability to release the therapeutic product. Such a microcapsule should be formed of oppositely charged polyelectrolytes, for example, alginate and poly-L-lysine. However, poly-L-lysine can have an adverse impact, and chitosan is a promising polyelectrolyte to replace it [45].

Cell technology utilizes chitin- and chitosan-based materials for biocompatible matrixes. These matrixes are highly adhesive to mesenchymal stem cells and promote proliferation and differentiation. They are particularly promising for human skin cells cultivation [51].

## 2.2. Ionic liquids

### 2.2.1. “Common” ionic liquids

Ionic liquid (IL) is an organic salt consisting entirely of ions and with melting point lower than 100 °C. Typical cations are bulky organic molecules of low symmetry containing positively charged nitrogen, sulfur or phosphorus atom (e.g. N, N'-dialkylimidazolium, N-alkylpyridinium, alkylammonium, alkylphosphonium, alkylsulphonium and diazolum cation), while anions can be inorganic or organic species such as halides (e.g. Br<sup>-</sup>, Cl<sup>-</sup>), tetrafluoroborate (BF<sub>4</sub><sup>-</sup>), hexafluorophosphate (PF<sub>6</sub><sup>-</sup>), bis(trifluoromethylsulfonyl)imide ((CF<sub>3</sub>SO<sub>2</sub>)<sub>2</sub>N<sup>-</sup>), acetate (CH<sub>3</sub>CO<sub>2</sub><sup>-</sup>) and dicyanamide (N(CN)<sub>2</sub><sup>-</sup>) [4, 5].

There are no general properties of ILs, apart from the abovementioned melting point below 100 °C, since ILs are a heterogeneous group of compounds and therefore possess diverse physicochemical properties [5, 21]. ILs have been considered to be a promising alternative to traditional organic solvents as environmental friendly and easy to obtain [4]. The areas of IL application include, but not limit to, metal processing, biodiesel synthesis, gas and azeotropic mixtures separation, pervaporation, catalysis, fabrication of “artificial muscles”,

usage as reaction media and electrolytes for fuel cells [6–10]. Some of these applications are reviewed in the next two sections in more detail.

However, the application of ionic liquids is shown to have numerous potential environmental risks [5, 21]. This results in a search for alternative solvents, which would have lower environmental impact while being able to perform the same functions.

### 2.2.2. Deep eutectic solvents

Compared to common ILs, deep eutectic solvents (DESs) emerged only a short time ago: the first paper on the subject was published in 2001 [22], the term “deep eutectic solvent” appearing two years later [23]. Since then DESs received much attention from the researchers.

A DES is a eutectic mixture formed when two or three components associate with each other via hydrogen bond interactions. A melting point of the resulting DES is lower than that of each individual component, typically below 150 °C, and for the majority of DESs the melting point lies between room temperature and 70 °C [24].

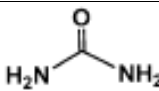
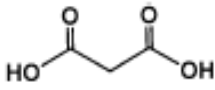
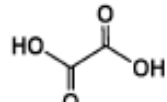
A DES is a combination of any ammonium, phosphonium or sulphonium cation with Lewis base (which is generally halide anion) and Lewis or Brønsted acid [25]. Smith et al. distinguish four types of DESs: (I) metal chlorides with quaternary ammonium salts, (II) hydrated metal halides with choline chloride, (III) chloride choline with hydrogen bond donors (HBDs) and (IV) organic cations with transition metals [25]. As DESs are not entirely composed of ionic species and can also be obtained from non-ionic species, they cannot be considered ILs [24]. The melting point depression, which is due to the charge delocalization, depends on the lattice energy of a DES and the way of anion-HBD interaction and it may be considered a measure of the entropy change arising when a liquid phase forms [8, 22].

Choline chloride (ChCl) is one of the most widely used quaternary ammonium salts due to its low cost, low toxicity and biodegradability. ChCl production is almost waste-free, since it is obtained by a one-step gas phase reaction between HCl, ethylene oxide and trimethylamine. ChCl forms a type III DES in combination with urea, carboxylic acids (e.g.

oxalic, malonic, citric, succinic or amino acids) or polyols (e.g. glycerol, carbohydrates); DESs of this type are particularly adaptable [24, 25].

Melting point of pure ChCl is 302 °C, and melting points of several choline-based DESs, as well as those of pure HBDs, are provided in the Table 1. Melting point depression compared to pure HBD is more than 100 °C.

Table 1. Melting point ( $T_m$ ) of the choline-based DESs.  $T_m^*$  is melting point of pure HBD.

Hydrogen bond donor (HBD)	ChCl : HBD (molar ratio)	$T_m$ , °C	$T_m^*$ , °C	Re f.
	urea 1:2	12	134	23
	malonic acid 1:1	10	135	8
	oxalic acid 1:1	34	190	8

Unlike those of ILs, components of DESs are cheap, renewable and biodegradable. In addition, the process of DES preparation is simple (components are merely mixed together) and does not require for purification and waste disposal. Another advantage of DESs is that they are chemically inert with water and therefore easy to store [24].

Since vapor pressure values of DESs are lower than those of ILs, levels of emission to the atmosphere are lower. However, owing to hydrogen bonds, DESs are partly miscible with water, which means their pathway may end in an aqueous environment [52, 53]. It should be noted that, although each of DES components may be safe, the resulting mixture possesses completely different properties, which questions the DES “greenness”. Hence, more thorough investigation of their environmental impact is needed, as well as a search for the recycling method [25, 53].

While having advantages over ILs, DESs possess physico-chemical properties close to those of common ILs, which allows for applications in the same areas [24]. Nevertheless, some DES properties differ from the IL properties. Compared to that of ILs, ionic conductivity of most DESs is poor (lower than 2 mS/cm at room temperature) due to their high viscosity [24]; however, DESs are better conductors than conventional organic

solvents [54]. For instance, for ChCl/urea ionic conductivity equals to 0.199 mS/cm at 40 °C [55] and for ChCl/malonic acid it equals to 0.55 mS/cm at 25 °C [54]. Generally DESs ionic conductivity increases with temperature as their viscosity decreases; it exhibits Arrhenius-like temperature behavior.

DESs are most widely applied in metal processing and as a synthesis media [24]; they are also utilized for nanotechnology [54], gas capturing [56] and polymer films modifications [26–30].

Metal electrodeposition proceeds in DESs without passivation, unlike that in aqueous and organic solvents, since metal salts as well as metal oxides and hydroxides are soluble in DESs. Another metal processing application of DESs is electropolishing, i.e. controlled dissolution of metal surface. As aluminates and silicates are insoluble in DESs, while metal oxides are soluble, metal ions could be extracted from aluminosilicate matrix without dissolving the matrix [8, 25].

Applications of DESs in nanotechnology include using them as a reaction media for nanomaterial production, which comprises physicochemical synthesis, nanomaterial electrodeposition and physical sputtering deposition [54]. In particular, a novel synthesis method — ionothermal synthesis — utilizes ILs or DESs both as solvents and potential templates, whereas in a traditional hydrothermal synthesis organic template is added to the mixture [25]. In addition, DESs can act as a media to disperse nanoparticles, i.e. prevent nanoparticle from agglomeration without surfactants usage, and control morphology [54]. Nanosized DESs can be used in solar cells, as lubricants and catalysts, as well as for assigning thermochromic properties to materials.

One of the crucial environmental issues is gas capturing, especially that of carbon dioxide. While traditional amine solvent-based technology has certain drawbacks, such as high energy consumption, insufficient CO<sub>2</sub>/H<sub>2</sub>S capture capacity and corrosive byproducts formation, ILs and DESs have been reported to be promising capturing agents [25, 56]. In particular, ChCl/urea eutectic mixture has been found to possess higher CO<sub>2</sub> capturing ability than ILs at room temperature. ChCl/lactic acid mixture is also a promising candidate for gas separation [57]. However, the potential of DESs for SO<sub>2</sub> absorption is limited [56].

Another environmental issue is the synthesis of biodiesel from renewable sources as an alternative to the fossil fuels. Both ILs and DESs can act as biodiesel synthesis catalysts and (co-)solvents for chemical or enzymatic reactions [25, 27], DESs having the aforementioned advantages over ILs.

DESs can be used for separation of azeotropic mixtures, particularly mixtures of alcohols and alkanes, which are not separable by simple distillation [58]. Oliviera et al. [58] studied ChCl/HBD mixtures as a media for ethanol/heptane liquid-liquid extraction, where one of the components is soluble in the extraction media and another is insoluble. DESs containing HBD with hydroxyl groups were shown to have better selectivity and DESs with carboxylic group in HBD had higher distribution coefficient, which means less amount of solvent required. It should be noted that all studied DESs possessed better parameters than ILs.

DESs are applied as a media for biotransformations, i.e. chemical modifications of a chemical compound made by enzyme or organism; DESs lack the main drawback of traditional aqueous organic solvents, which is enzyme deactivation by polar organic solvents [25]. Transformations of unprotected sugars, cellulose and starch are also possible in DESs; in addition, DESs act as plasticizers for starch, cellulose acetate and other biopolymers [25, 26–30].

Paiva et al. [53] report biomedical applications of natural DESs, consisting of primary metabolites. DESs can dissolve model drugs, increasing solubility, permeation and absorption. A combination of a natural DES with a biopolymer may serve as a drug delivery system.

### 2.3. Polymer/IL and polymer/DES composites

An example of the polymer/IL application is provided by the supported ionic liquid membranes (SILMs) for biobutanol pervaporation [16, 17]. A conventional microbial production of biobutanol possesses such drawbacks as low efficiency and high cost. Liquid-liquid extraction with ILs as extractants is promising due to ILs extraction properties; however, it is also cost intensive and requires for the product recovery. Pervaporation using SILMs enable the continuous product removal, thus overcoming these

limitations. SILM is a polymer membrane where the IL is immobilized in pores; stable immobilization is crucial for the pervaporation process. The separation characteristics of the SILMs can be tuned by varying the type and quantity of the immobilised IL. For instance, Heitmann *et al.* [17] tested three ILs: 1-decyl-3-methylimidazolium tetracyanoborate ( $\text{Im}_{10,1} \text{ tcb}$ ), trihexyltetradecylphosphonium tetracyanoborate ( $\text{P}_{6,6,6,14} \text{ tcb}$ ) and 1-decyl 3-methylimidazolium tris(pentafluoroethyl) trifluorophosphate ( $\text{Im}_{10,1} \text{ fap}$ ). The study showed  $\text{Im}_{10,1} \text{ tcb}$  to be the most suitable for pervaporation among these ILs, since the highest permeate flux was obtained for SILMs with this IL. Rdzanek *et al.* [16] also studied  $\text{Im}_{10,1} \text{ tcb}$  and  $\text{P}_{6,6,6,14} \text{ tcb}$  and revealed the dependence of the permeation properties on the immobilization arrangement.

An application of SILMs for gas separation has also been studied [11–13]. Scovazzo *et al.* [11] tested bis(trifluoromethanesulfonyl)amide  $[\text{Tf}_2\text{N}]^-$ , trifluoromethanesulfone  $[\text{CF}_3\text{SO}_3]^-$ , chloride  $[\text{Cl}]^-$ , and dicyanamide  $[\text{dca}]^-$  for acid gas separation, specifically  $\text{CO}_2$  from  $\text{N}_2$  and  $\text{CO}_2$  from  $\text{CH}_4$ . Previously, the usage of hexafluorophosphate  $[\text{PF}_6]^-$  anion has been reported; however, it has a drawback of possible breaking down into HF in the presence of water [12]. SILMs with  $[\text{Tf}_2\text{N}]^-$  were shown to exhibit the highest  $\text{CO}_2$  permeability. Park *et al.* [13] showed 1-butyl-3-methylimidazolium tetrafluororate ( $\text{BMImBF}_4$ ) and poly(vinylidene fluoride) SILMs to be suitable for the removal of  $\text{CO}_2$  and  $\text{H}_2\text{S}$  from natural gas. Jiang *et al.* [14] studied  $\text{SO}_2$  gas separation with imidazolium-based ILs supported on the polyethersulfone microfiltration membranes. These SILMs exhibited good  $\text{SO}_2$  permeability and high  $\text{SO}_2/\text{CH}_4$  and  $\text{SO}_2/\text{N}_2$  selectivities;  $\text{CO}_2$  permeability and selectivity in tested membranes were one order of magnitude lower.

While ILs possess clear advantages over traditional organic solvents for pervaporation and gas separation, namely, negligible vapor pressure, which minimizes solvent loss, and tunability [11, 15], SILMs cannot withstand pressure over a few bar, IL being pushed through the support pores at industrial pressure values [15]. At elevated temperatures this problem becomes more acute since the liquid viscosity decreases and the polymer support mechanical strength reduces. One solution to this problem is provided by composite ionic liquid and polymer membranes (CILPMs), where IL is trapped within the polymer membrane, which eliminates the solvent loss at high pressure [15]. However, to achieve the desirable permeability, higher temperatures should be used, which requires for thermally stable materials. Liang *et al.* [15] showed polybenzimidazole- and polyimide-

based CILPMs with 1-butyl-3-methylimidazolium bis(trifluoromethylsulfonyl)imide ([C<sub>4</sub>mim][NTf<sub>2</sub>]) to display a significant potential for gas separation applications.

Polymer/IL composites have also been applied for “artificial muscles”, i.e. electroactive polymers (EAPs) that exhibit large bending deformation in response to electrical stimulation [10, 18–20]. Bacterial cellulose (BC) is an interesting electroactive biopolymer; however, BC-based artificial muscles show relatively low ionic exchange capacity, low ionic conductivity, high mechanical stiffness, and low actuation performance compared with other synthetic ionic polymer actuators [10, 18]. Wang et al. [10] used carboxylated bacterial cellulose (CBC) with IL incorporation. As a result of the strong ionic interaction between the carboxylic acid groups of CBC and IL, the CBC-IL actuator exhibited higher ionic exchange capacity, ionic conductivity and tuned mechanical properties. Therefore, it showed large bending deformation under both step and harmonic electrical inputs (4.9 mm under an applied DC-voltage of 2.5 V and ±0.8 mm under a peak voltage of 2 V at 0.5 Hz) [10]. The actuator’s performance and durability were further improved in [18] by adding a highly conductive ionic polymer poly(2-acrylamido-2-methyl-1-propanesulfonic acid) (PAMPS), the hydrophilic sulfonate functional groups of which can act as ion exchange sites and proton donors. Another polymer, Nafion N117, was used for fabrication of artificial muscles by Okazaki et al. [20], and the study showed that usage of IL instead of water led to a bending ability remaining unchanged for a long time regardless of the atmospheric humidity.

Although polymer/IL composites are significantly more studied than composites with DESs, there are a number of articles on polymer/DES composites. The most interesting are those based on natural polymers. Several researches showed DESs and ILs to act as plasticizers for starch [26–28, 59] and agarose [29, 30] films. Plasticization enhances polymer plasticity and/or elasticity and decreases the glass transition temperature  $T_g$ . As a result, a plasticized polymer can be processed by common methods such as thermo-compression molding [26, 31].

Choline-based DESs [26–28] and ILs [59] have been used for starch modification. Incorporation of DESs into starch strengthened the material, improved its flexibility and led to the plasticization.  $T_g$  determined by Abbott et al. [26] equaled to -16 °C for 50 wt% content of ChCl/urea and 24 °C for 30 wt%. Leroy et al. [27] also showed ChCl/urea to act as a plasticizer: the characteristic temperature of the  $\alpha$ -relaxation associated with glass

transition equaled to 32 °C. For starch modified with ChCl/glycerol, also studied in [27], this characteristic temperature equaled to 42 °C. Colomines et al. [59] used cholinium-based ILs with different anions (acetate, saccharinate, salicylate, citrate, lactate and furoate) for starch modification, which led to the  $T_g$  of the resulting material being in the range from -6 to 20 °C. The structure of the anion was shown to have a considerable effect on thermo(hydro)mechanical behavior of the modified starch.

Apart from plasticization and mechanical properties improvement, DESs were shown to enable starch compatibilization with a hydrophobic phase, e.g. polyethylene [28]. Blending of polyolefin based plastics with carbohydrate based polymers accelerates plastic degradation; however, it is not possible without modification, which is usually chemical, while modification with DESs is non-chemical.

Choline-based DESs were also shown to improve physicochemical and mechanical properties of agarose films [29, 30]. Importantly, ChCl/urea mixture is non-acidic, whereas acidic solvent could hydrolyze the agarose. Shamsuri and Daik [29] investigated agarose films with 30 to 70 wt% of ChCl/urea. While glass transition temperature ( $T_g$ ) for pure agarose was observed at 105.3 °C, modified agarose films exhibited  $T_g$  from 70.2 to 6.3 °C,  $T_g$  depression increasing with ChCl/urea content. In addition, agarose films containing ChCl/urea exhibited no surface roughness and no phase separation, which gives further evidence to ChCl/urea being a successful plasticizer for this polymer. Mechanical properties were also improved; agarose films containing ChCl/urea possessed higher tensile extension and tensile strain properties, the best results being achieved for 60 wt% content, while tensile stress and modulus decreased in comparison with pure agarose. In addition, modified films were more optically transparent than pure agarose films. Sousa et al. [30] also showed that using DESs (ChCl/urea or ChCl/glycerol) for agarose film production enhanced films elasticity and mechanical resistance.

The composites of chitosan with DESs are almost unexplored; to the best of our knowledge, only one study addresses this issue [31]. This article reports an application of ChCl and citric acid deep eutectic mixture for chitosan film mechanical properties improvement. Chitosan films prepared with citric acid (CA) only and with ChCl/CA mixture were compared, and those with DES were shown to possess better mechanical properties (they were less elastic, but exhibited higher elongation at break and lower Young modulus).

### **3. Objectives of this work**

This work aims to determine the compatibility of DES based on the choline chloride and malonic acid with chitosan and to investigate the influence of the DES content in the chitosan/DES composites on the surface morphology, nanomechanical and electrical properties. In order to achieve this goal, the following objectives were formulated:

- 1) To prepare a set of films with various content of DES;
- 2) To obtain morphology maps by means of AFM spectroscopy;
- 3) To investigate the films homogeneity by Young's modulus and adhesion mapping;
- 4) To determine the films micro-scale response to the electric field.

## 4. Methodical part

### 4.1. Scanning probe microscopy: Basic principles

Scanning probe microscopy (SPM) is a powerful technique for high-resolution solids surface morphology and properties investigation, which in nowadays widely applied [60]. SPM devices include scanning tunneling microscope (STM), atomic force microscope (AFM), magnetic force microscope (MFM), scanning electrostatic force microscope (SEFM), scanning near field optical microscope (SNOM) and others.

All SPM devices are based on the general principles. The surface study is carried out by using the needle-shaped probe, which has the tip radius of about 10 nm. Various interactions between probe and surface allow SPM devices to determine surface relief and local properties. Suppose interaction between the probe and the surface is characterized by some parameter  $P$ ; if the relation  $P = P(z)$  between this parameter and probe-sample distance  $z$  is bijective and sufficiently sharp, this parameter can be used for a feedback system controlling probe-sample distance.

### 4.2. Atomic Force Microscopy

Atomic Force Microscopy (AFM) is an experimental method of surface properties determination based on the Van der Waals interaction between a solid probe tip and a sample's surface. Different tip-sample interaction types allow for the measurements of the local parameters of topography, surface potential, mechanical properties (stiffness, adhesion, friction), magnetic properties etc.

The main elements of AFM scheme are as follows: 1) probe (sharp tip) attached to a flexible cantilever; 2) piezo-scanner used to move the sample relative to the tip; 3) optical detection system (laser and 4-sectional photodetector), detecting the bending angle of cantilever; and 4) feedback system. These elements are described in more detail further in this section. There are also additional components such as measurement electronic unit, personal computer, vacuum pump, vibration isolation table etc.

The operational principle of the AFM is depicted in Figure 1. The surface roughness is registered by the flexible console called "cantilever" which ends with a sharp tip. The cantilever bends due to the force created by the surface roughness, and the photodetector

registers the bending angle by the shift of the reflected laser beam (the difference between light falling on different sections of the photodetector is calculated). This angle is recorded at each point and the tip's trajectory profile is displayed as the scanned line.

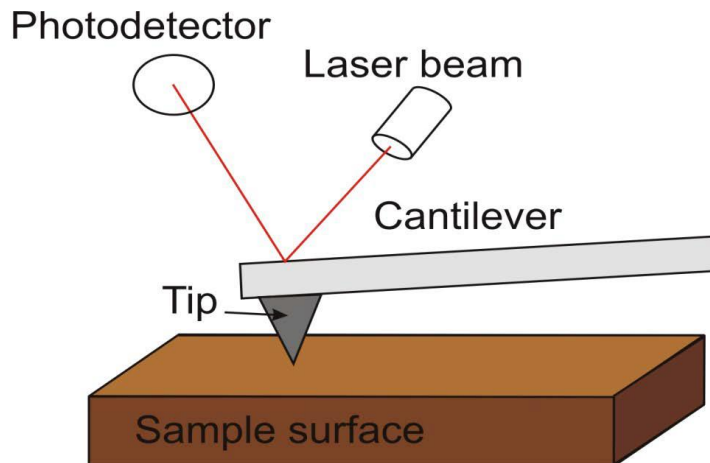


Figure 1. Operational principle of AFM [Image courtesy of Connexions®, Rice University, USA].

Probe-surface interaction is described by the Lennard-Jones potential, which takes into account repulsive and attractive interactions (Figure 2). The left part of the curve corresponds to the contact mode AFM measurements, when the tip is in direct contact with the surface, pressing on it. The applied pressure is controlled by the system parameter “SetPoint” so that the tip does not destruct the surface. Right part of the curve corresponds to the non-contact mode, when the probe tip oscillates near the surface. This mode is usually used as a part of a “two-pass” technique. The surface topology is measured in the first pass, and then the tip is lifted up and the constant distance is maintained during the second pass based on the measured topology. This second pass allows for measurements of the strong long-range forces, such as electrostatic or magnetic.

LENNARD-JONES potential

$$V(d) = 4\epsilon \left( \left( \frac{\sigma}{d} \right)^{12} - \left( \frac{\sigma}{d} \right)^6 \right)$$

repulsion (short range)
attraction (long range)

$\epsilon, \sigma = \text{const}$

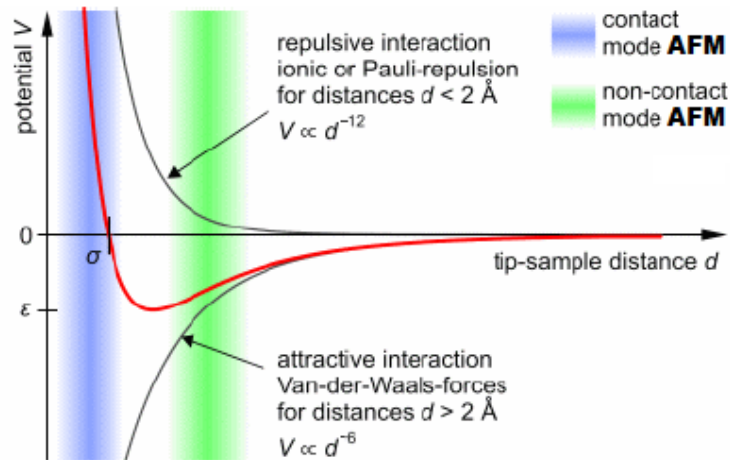


Figure 2. Lennard-Jones potential [61] [Image courtesy of Soft Matter Physics Division, University of Leipzig, Germany]

Between these regions there is also an area of semicontact, or tapping, mode (Figure 3). In this mode the tip is oscillating and “rattling” the surface. Initially it oscillates with cantilever’s resonant frequency not touching the surface. When the tip-sample distance decreases, growing repulsive force is diminishing the oscillations amplitude. The feedback system is then distracting the sample from the tip so that the amplitude returns to the initial value. Whereas the contact mode is not applicable to the living cells or other soft samples due to the significant forces, the semicontact mode can be used for such samples because the impact on the surface is much less.

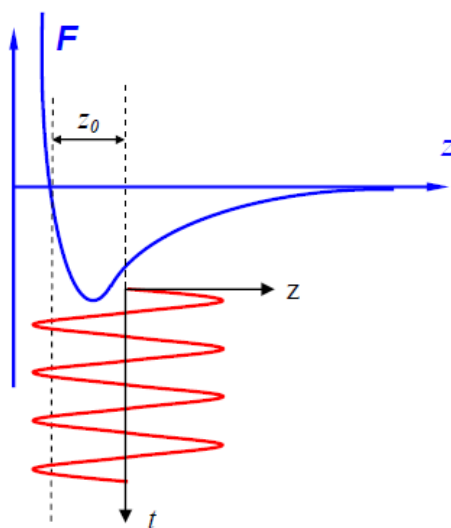


Figure 3. Distance in Semicontact mode [60].

AFM image is a two-dimensional map which shows the values of the measured surface parameter for each pixel of the image. The measurement is performed line by line, the tip going firstly in one direction, then back, “rising up” and passing through the next line (Figure 4). Data are recorded in the straightway.

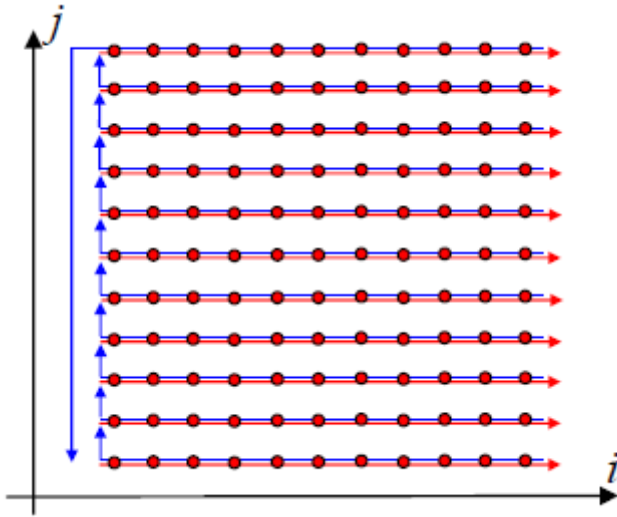


Figure 4. Scheme of scanning process: red is straightway, blue is reversal ( $j$  is number of pixel line,  $i$  is number of position) [60].

For better understanding of AFM performance it is necessary to describe its main elements (probe; piezo-scanner; optical detection system; feedback system) in more detail.

Probe is usually a sharp tip of pyramidal form fixed on a flexible cantilever. Probes are made of polysilicon or  $S_3N_4$ . The main parameters characterizing the tips are 1) tip's apex radius (usually called as tip radius  $r$ ); 2) cantilever spring constant  $k$ , and 3) cantilever resonant frequency  $w$ .

Tip radius  $r$  is the critical parameter limiting the lateral resolution of AFM scanning. For Si tips without additional coatings  $r = 2$  nm and for coated tips it can reach 30 nm. While decreasing the resolution, tip coatings provide such possibilities as electrical or magnetic properties measurements.

Spring constant of cantilever  $k$  ranges from 0.01 N/m to 225 N/m [62, 63].  $k$  is related to the magnitude of displacement of the tip height  $\Delta Z$  and force  $F$  by equation  $k = F/\Delta Z$ . Probes with small  $k$  values (0.01 – 0.03 N/m) are used for measurements on living cells

and other delicate samples. Large  $k$  values are used in semicontact mode, where the force magnitude is less.

The resonant frequencies of cantilever  $w$  range from 10 to 1000 kHz. Quality factor which is a measure of energy loss of oscillation is related with  $w$ .

Piezo-scanner is a device that moves the sample relatively to the probe or vice versa. Since the measurements are more accurate when the optical system is not moving, scanner is usually attached to the sample holder (although it can be said for the sake of simplicity that “tip rises up” or “tip approaches to the surface”). Scanner consists of a radially polarized piezoceramic tube and metal electrodes on the four sides. When the voltage is applied, the piezoelectric effect makes tube bend or stretch/shrink, thus allowing for sample movements in three directions.

Piezoceramics inherently possesses drawbacks that should be taken into account: nonlinearity, creep and hysteresis (Figure 5). Nonlinearity of piezoceramics (Figure 5 a) appears as a deviation from the linear dependence of the piezocrystal length at unit voltages over 100 V/mm. Creep (Figure 5 b) is a delay in response to the controlling voltage  $V$ . This usually reveals in a white strip in the left side of the image; usually the software crops this first point and does not visualize it. Hysteresis properties of piezoceramics (Figure 5 c) are the reason why the data is different for straightway and reversal pass and why measurement is done only in one direction.

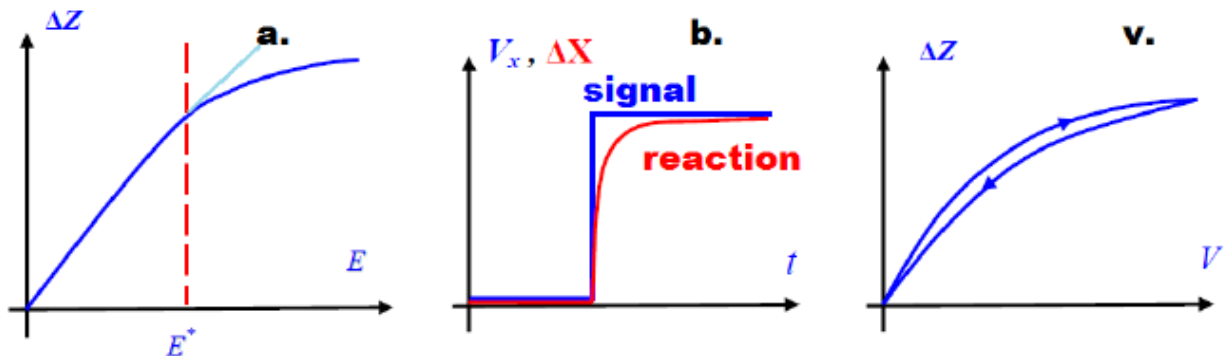


Figure 5. Piezoceramic drawbacks: a. nonlinearity; b. creep; c. hysteresis [60].

Optical detection system measures the cantilever deflection caused by the force in the AFM tip during the scanning process. It consists of a laser source pointing a beam onto a cantilever and a 4-sectional photodiode measuring the intensity of laser light reflected from

the cantilever to each of its four sections. To improve the reflection, the cantilever may be coated with a thin metal film on its back side.

Prior to the measurements the system is adjusted so that laser beam falls onto the cantilever and is reflected to the exact center of the photodetector, the intensity of light falling on each section being the same. When cantilever bends due to an additional force, the angle of the reflected laser beam changes and the laser spot at the photodetector is shifted. These small shifts are measured by the difference in photocurrent from different sections, and then the tip-surface interaction force is determined.

Feedback system maintains a constant influence on the probe.

#### 4.3. PeakForce QNM<sup>®</sup> mode

While surface topography alone is important, surface mechanical properties at nanoscale are of great interest. Bruker company developed an imaging mode that enables quantitative mechanical properties mapping with high resolution — PeakForce QNM (Quantitative Nanomechanical Properties Mapping) mode [36]. Previously existing techniques possess significant drawbacks; for example, HarmoniX<sup>®</sup>, although successfully resolving material components in complex polymer system, required special probes, and both operation and interpretation of the results were difficult. PeakForce QNM lacks these drawbacks. Apart from providing high-resolution mapping of mechanical properties, it is also non-destructive to tips and samples and it provides unambiguous and quantitative data for a broad range of parameters.

PeakForce QNM implements a novel Peak Force Tapping<sup>®</sup> technology, where the probe is periodically modulated at about 2 kHz. In Peak Force Tapping the tip and the sample are in contact only for a short time, which eliminates lateral forces that could cause damage to the tip or the surface, and the tip-contact area is minimized. This technology controls the maximum force (Peak Force) on the tip.

Figure 6 (i) demonstrates the interaction between the periodically modulated probe and the sample. The blue solid line represents the measured force during the approach, while the red line represents the force while the tip is distracted from the surface. When the tip is far from the surface (point A), only long range forces affect the tip, so the force is very small

or zero. As the tip approaches the surface, the cantilever is pulled down toward the surface by attractive forces (usually van der Waals, electrostatics, or capillary forces), so the force is negative. At point B, the attractive forces overcome the cantilever stiffness and the tip is pulled to the surface; this point is called “jump-to-contact”. The tip then stays on the surface and the force increases until the Z position of the modulation reaches its bottom-most position at point C, and this is where the peak force occurs. The peak force during the interaction period is kept constant by the system feedback. The probe then starts to withdraw and the force decreases until it reaches a minimum at point D. The adhesion is given by the force at this point. The point where the tip comes off the surface is called the pull-off point. When the tip is again far from the surface (point E), there is little or no force.

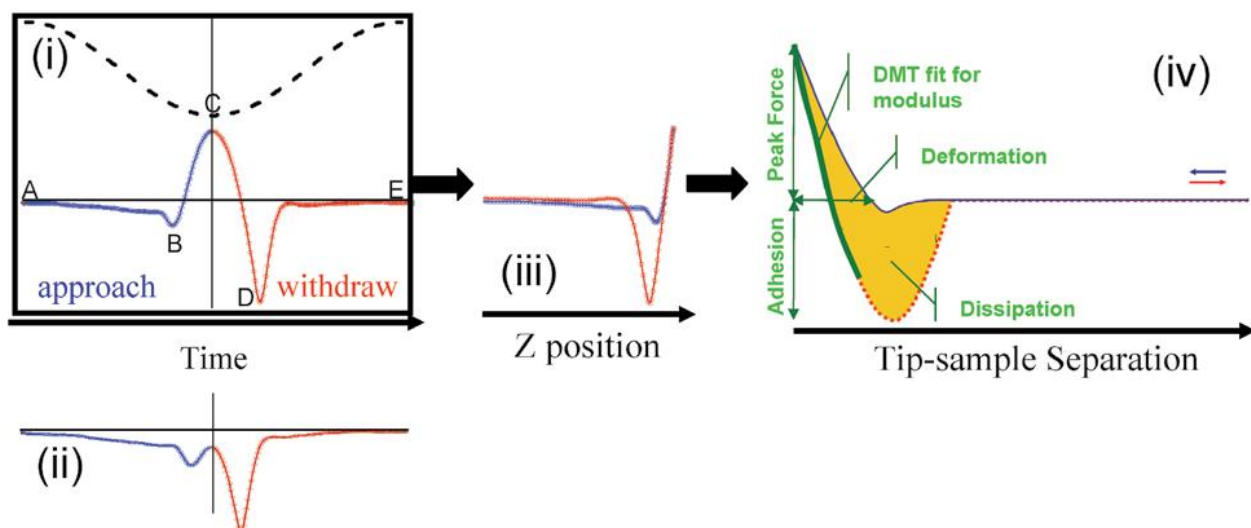


Figure 6. Force curves: (i) Plot of force (solid line) and piezo Z position (dashed line) as a function of time; (ii) Plot of force vs. time with small peak force; (iii) A traditional force curve eliminates the time variable, plotting Force vs. Z piezo position; (iv) Force-separation plot and the parameters that can be obtained [36].

If the peak force is small and the attractive forces are large, it may happen that the forces are negative during the whole interaction and the force at point C is not the maximum force (Figure 6, ii). However, Peak Force Tapping still can recognize the local maximum and maintain control of the imaging process.

Another possible complication is the excitation of the cantilever resonance at the pull-off point, which is negligible for a stiff cantilever, such as the one used in figure 6, but which

can be significant for softer cantilevers. Having the ability to identify the repulsive force, Peak Force Tapping does not respond to the pull-off ringing.

The time variable can be eliminated to plot the force against the Z-position (Figure 6, iii). The resulting plot can be compared with the traditional force-distance curves obtained in previous investigations.

The curve obtained is converted to a force versus separation plot for fitting and further analysis (Figure 6, iv). The tip-sample separation is calculated from the Z piezo position and the cantilever deflection. The most common quantities that can be obtained are elastic modulus, tip-sample adhesion, energy dissipation, and maximum deformation.

The ability of the system operation in PeakForce QNM mode to acquire and analyze the individual force curves from each tap is what makes possible the material property mapping. To separate the contributions from different material properties it is necessary to measure the instantaneous force on the tip rather than a time-average of the force or dissipation over time. This requires a force sensor that has significantly higher bandwidth than the frequency of the periodic interactions. In Peak Force Tapping, the modulation frequency (2 kHz) is intentionally chosen to be significantly lower than the cantilever resonant frequency (10 – 1000 kHz). As a result, a properly chosen cantilever is able to respond to changes in instantaneous interaction force with an immediate deflection change.

The force-separation plots (Figure 6, iv) are analyzed to obtain the properties of the sample (adhesion, modulus, deformation, and dissipation) and the information is sent to one of the image data channels while imaging continues at usual imaging speeds. The result is images that contain maps of material properties (false colored with a user selectable color table). Since the system can acquire up to eight channels at once, it is possible to map all of the currently calculated properties in a single pass.

To obtain the Young's Modulus, the retract curve is fit using the Derjaguin–Muller–Toporov (DMT) model [64]:

$$F - F_{adh} = \frac{4}{3} E^* \sqrt{R(d - d_0)^3} \quad (1)$$

$F - F_{adh}$  is the force on the cantilever relative to the adhesion force,  $R$  is the tip end radius, and  $d - d_0$  is the deformation of the sample. The result of the fit is the reduced modulus  $E^*$ , which is related to a sample modulus, sample modulus and Poisson ratio.

PeakForce QNM provides quantitative modulus results over the range of 700kPa to 70GPa provided the appropriate probe is selected and calibrated, and provided that the DMT model is applicable. If the DMT model is not appropriate, the modulus map will still return the fit result, but it will be only qualitative. Some cases where the DMT model is not appropriate include cases where the tip-sample geometry is not approximated by a hard sphere (the tip) contacting an elastic plane, cases where mechanisms of deformation other than elastic deformation are active during the retracting part of the curve (at these time scales), and cases where the sample is confined vertically or laterally by surrounding material (close enough to effect the strain in the deformed region). One of the alternative models is Sneddon model which is often more appropriate for biological samples [35].

The adhesion is illustrated by the minimum force in figure 6 (iv). The source of the adhesion force can be any attractive force between the tip and sample, such as van der Waals and electrostatics forces and forces due to the formation of a capillary meniscus. The area below the zero force reference (the horizontal line in the force curve) and above the withdrawing curve is referred to as “the work of adhesion.”

The energy dissipation is given by the force times the velocity integrated over one period of the vibration (represented by the gold-coloured area in the figure 6 (iv)). The integration is zero if the loading and unloading curves coincide. For pure elastic deformation there is no hysteresis between the repulsive parts of the loading-unloading curve, so the energy dissipation is dominated by work of adhesion.

The maximum deformation is defined as the penetration of the tip into the surface at the peak force, after subtracting cantilever compliance. As the load on the sample under the tip increases, the deformation also increases, reaching a maximum at the peak force. The measured deformation may include both elastic and plastic contributions. Maximum sample deformation is calculated from the difference in separation from the point where the force is zero to the peak force point along the approach curve (see figure 6 (iv)). There may be some error in this measurement due to the fact that the tip first contacts the surface at the jump-to-contact point (figure 6 (i), point B) rather than at the zero crossing.

#### 4.4. PeakForce TUNA mode

Apart from measuring a range of mechanical properties, AFM method allows for a nanometer-scale electrical characterization of the surface. The AFM-based conductivity

measurements are categorized into two classes: Conductive AFM (CAFM), which covers the higher current range (sub-nA up to  $\mu\text{A}$ ), and Tunneling AFM (TUNA), which covers the lower current range (sub-pA up to nA). TUNA techniques include Contact Mode Based TUNA (Contact TUNA), TappingMode Point Contact IV (Tapping-TUNA), Torsional Resonance TUNA (TR-TUNA<sup>TM</sup>) and PeakForce TUNA (PF-TUNA) [37].

PF-TUNA is a Bruker's development of the TUNA technique based on Peak Force Tapping, which also has the capability of PeakForce QNM. It is able to perform precise tip-sample force control, which is ideal for soft delicate samples, and correlated nanoscale electrical property characterization through TUNA, and the ScanAsyst<sup>TM</sup> image optimization algorithms ensure the ease of use.

An operational frequency of Peak Force Tapping is 1 – 2 kHz, and the time of tip-sample contact in each tapping cycle is as small as tens to hundreds of microseconds. In order to be able to register a current signal during this time period with acceptable signal-to-noise ratio, the sensing module must have the bandwidth 10 times greater than the tapping frequency at the chosen gain. The TUNA sensing module has this capability due to a bandwidth around 15 kHz across a range of gains from  $10^7$  V/A to  $10^{10}$  V/A, with the noise below 100fA on cycle-averaged current.

Figure 7 illustrates the interaction of the periodically modulated PeakForce Tapping probe with the surface. The top and the middle line represent the time dependences of Z-position of the cantilever base and the force measured by the probe during the approach (blue) and withdraw (red) of the tip to the sample, respectively. The bottom line (green) represents the detected current passing through the sample.

Three measurements are extracted from the current-time plot by the PeakForce TUNA algorithm: 1) peak current, 2) cycle-averaged current, and 3) contact-averaged current. Peak current is the instantaneous current at point C, coinciding with peak force, which corresponds to the current measured at a defined force. Peak current is not necessarily the maximum current, since the limited rise time (imposed by the bandwidth of the TUNA module or the resistance-capacitance of the sample) may cause a lag in the current response. Cycle-averaged current is the average current over one full tapping cycle, from point A to point E, and it includes both the current measured while tip is in contact with the

surface, and while it is off the surface. Contact-averaged current is the average current over the time of tip-surface contact, from the snap-in at point B to the pull-off at point D.

The current-time plot does not always have a peak (as in the force-time plot); current can reach a plateau after a certain force threshold. There is also an AC current component of the measurement, part of which is capacitive charging, which is removed from the output. The tip (including cantilever) and the sample essentially form a capacitor, and the modulation of z-position causes its capacitance to modulate. At a constant DC bias, charging/discharging current at the tapping frequency will occur. Again, this is considered parasitic, and removed as background.

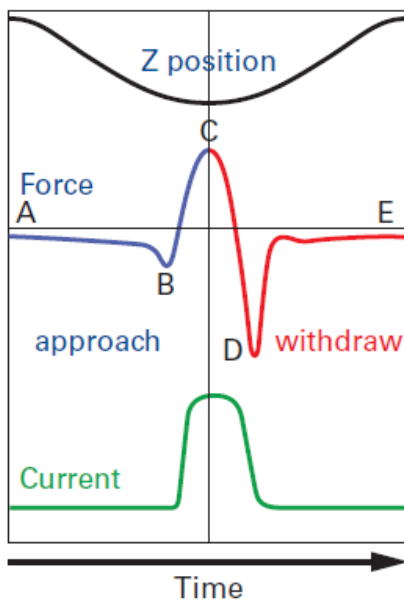


Figure 7. Plots of Z position, Force and Current as a function of time during one PeakForce Tapping cycle, with critical points labeled [37].

PeakForce TUNA can be operated in either imaging or spectroscopy mode. In the imaging mode, maps of the electrical current are obtained with topography and mechanical properties. The spectroscopy mode allows for current-voltage (I-V) curves measurements.

In the imaging mode, an electrically conductive probe is scanned over the sample surface in PeakForce Tapping mode as the feedback loop maintains the constant value of the maximum force (peak force) applied to the tip. During scanning, a DC bias can be applied between the tip and the sample. The TUNA module senses the resulting current passing through the sample, and this data is presented simultaneously with the topography image

and mechanical properties maps (when using PeakForce QNM). The observed current can be used as a measure of the local conductivity, or electrical integrity, of the sample under study. Since the system can acquire up to eight channels simultaneously, it is possible to map the major mechanical properties and electrical properties together with topography in a single pass.

In the I-V spectroscopy mode, the imaging scan is stopped and the tip is held in a fixed location while the sample bias is ramped up or down. The feedback is switched to Contact Mode and a constant deflection is maintained by the feedback loop, which assures tip-sample contact is fixed while I-V curve is taken. The resulting current through the sample is plotted versus the applied bias. The software can either record a single spectrum or average over multiple spectra. Higher bandwidth of the PeakForce TUNA module allows I-V curves to be taken at higher speeds. The “Point & Shoot” feature allows the user to register I-V curves in a few spots of interest at specific regions on the sample. This feature offers the option of drawing a line or a box on an image, defining a number of points, and then the AFM tip automatically moves to those locations to capture one or multiple I-V curves at each point.

## 5. Experimental

### 5.1. Samples preparation

To obtain composite membranes based on chitosan and DES, choline chloride and malonic acid were taken in a 1:1 molar ratio and mixed together. Chitosan flakes were added to the mixture in a calculated amount, so that the weight content of DES based on choline chloride and malonic acid equaled to 33, 50, 67, 75 and 82%. Then the water was poured in the mixture, and it was stirred at the elevated temperature until complete dissolution. To obtain films of pure chitosan, chitosan flakes were dissolved in a weak water solution of acetic acid.

The films were prepared by a solution casting method. The solution was poured onto the Petri dish and dried. The obtained membranes had thickness of about 30  $\mu\text{m}$ .

### 5.2. Measurements

This section describes basic operational principles of Bruker Multimode 8 AFM. Measurements and data operating are conducted via “Nanoscope” software package.

Preliminary, all the equipment should be turned ON and warmed up for few minutes.

1) Probe selection. The probe should be chosen according to the operation mode and the anticipatory information about the sample. In this work, topography and mechanical properties were measured with the NCHV-A probe — a Bruker silicon probe with aluminum reflective coating, which is suitable for imaging in TappingMode™ and non-contact mode in air. Conductivity measurements were performed using HA\_FM/W<sub>2</sub>C probe (ScanSens probe with tungsten carbide coating) and PF-TUNA probe (Bruker probe with platinum/iridium coating). The label parameters of these probes are specified in table 2 [62, 63].

Table 2. Label parameters of the used probes.

probe	NCHV-A	HA_FM/W <sub>2</sub> C	PF-TUNA
cantilever's shape	rectangular	rectangular	triangular
tip height	10–15 $\mu\text{m}$	$\geq 10 \mu\text{m}$	2.5–8.0 $\mu\text{m}$
tip radius	10 nm	< 35 nm	20 nm
cantilever's length	125 $\mu\text{m}$	223 $\mu\text{m}$	115 $\mu\text{m}$

cantilever's width	40 $\mu\text{m}$	34 $\mu\text{m}$	25 $\mu\text{m}$
resonant frequency	320 kHz	77 kHz	70 kHz
spring constant	42 N/m	3.5 N/m	0.4 N/m

2) Probe and sample installation. Installation of the probe and the sample are manually performed procedures, which require for carefulness and precision.

The probe is taken from its box with an adhesive coating in the bottom and installed in the probe holder with the help of tweezers. The holder is then mounted in the measuring head over the piezo-scanner.

The sample is placed onto a special plate (substrate) and fixed with the help of adhesive tap. The plate is put onto the scanner (without applying pressure to the piezo-tube) and electrically grounded. Then the measuring head with the probe holder is approached to the sample with the help of head's screws until the distance is about 3 mm. It is important not to touch the surface with the tip as it can cause tip damage.

In the case of conductivity measurements, the sample should be fixed on the substrate with the help of silver conductive paste and the probe holder should be connected to the electrical circuit, which is represented in Figure 8 in a simplified form. The resistances of the probe, silver conductive plate and substrate ( $R(\text{probe})$ ,  $R(\text{silver paste})$  and  $R(\text{substrate})$ , respectively) can be neglected, and the unknown  $R(\text{contact})$  — the resistance of the contact between probe tip and sample — is not taken into account. Thus, the device is assumed to measure the resistance of the sample. In fact, the sample may also possess inductance and capacity.

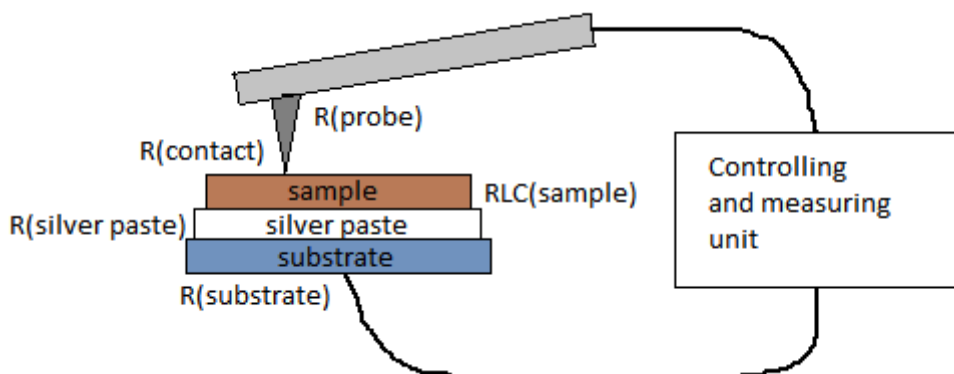


Figure 8. A simplified electric scheme of the conductivity measurement.

3) Setting the probe. Before starting the measurement, a laser should be pointed onto the cantilever. Firstly, an optical microscope is focused on the probe. Then the laser spot is moved onto the probe's end with the help of a laser sensor's screws. The detected value of the laser light should be the maximum possible; this position is found with the help of photodetector's screws.

4) Starting the measurement. When the operation mode is selected, the probe should be approached to the surface and the necessary parameters should be set.

The probe approaching should be done carefully in order not to damage the probe tip. The optical microscope is focused on the surface sample and the probe is approached to the sample surface manually with the help of measuring head's screws. When the probe is visible rather clearly in the optical microscope image, which means it is close to the surface, the rest of the approach is done automatically by the software.

During the measuring setting the following parameters are selected: the scanning area, the scanning speed, the resolution (number of pixels per scan), the force between probe and surface and the characteristics that will be displayed.

## 6. Results

The bulk measurements in uniaxial extension mode revealed the Young's modulus values tabulated in Table 3. We expected to distinguish in the AFM images the regions of high and low Young's modulus, corresponding to phases of different composition, which would give information about the DES localization.

Table 3. Young's modulus obtained in the uniaxial extension mode

content of DES, %	0	33	50	67	75	82
Young's modulus, MPa	2500	1700	300	29	25	15

Since pure chitosan is non-conductive, while macroscopic research showed composites of chitosan with DES to be conductive, we expected to obtain the conductivity maps, also demonstrating the DES localization.

### 6.1. Topography

Premised on the preliminary data on Young's modulus values, we chose the NCHV-A probe with label spring constant 42 N/m (suitable for measuring moduli ranging from 200 to 2000 MPa) for measurements in PeakForce QNM mode. During the calibration process the following probe parameters were determined: spring constant 41.13 N/m and tip radius 150 nm. Peak Force Setpoint was set to 20 nN.

The average vertical deformations during the scanning process are presented in Table 4; however, in some regions of the sample with 82% of DES deformation was up to several tens of nanometers. The optimal deformation value is equal to 1 nm. The obtained deformation values variation is due to different sample stiffness.

Table 4. Average vertical deformations for samples with different DES content

DES content, %	deformation, nm
0	0.45
33	0.52
50	0.94
67	2.36
75	2.91
82	8.20

PeakForce QNM measurements were carried out for upper and lower sides of all samples. Here the scans of lower side are presented, unless otherwise stated. The scan sizes were 3  $\mu\text{m}$  and 10  $\mu\text{m}$ .

Integration of the DES into a chitosan matrix was shown to result in the morphology changes (Figure 9, 10). The pure chitosan surface was smooth, whereas the islands of fiber-like structures were present on the DES-containing film surfaces, the island size diminishing with DES content increase. Based on the 3  $\mu\text{m}$  image, the fiber diameter was evaluated to be 45 – 50 nm for the sample with 50% of DES. For other samples it was of the same order of magnitude. Surface roughness was also calculated as the root mean square deviation  $R_q$  (Table 5) based on 3 and 10  $\mu\text{m}$  topography images.

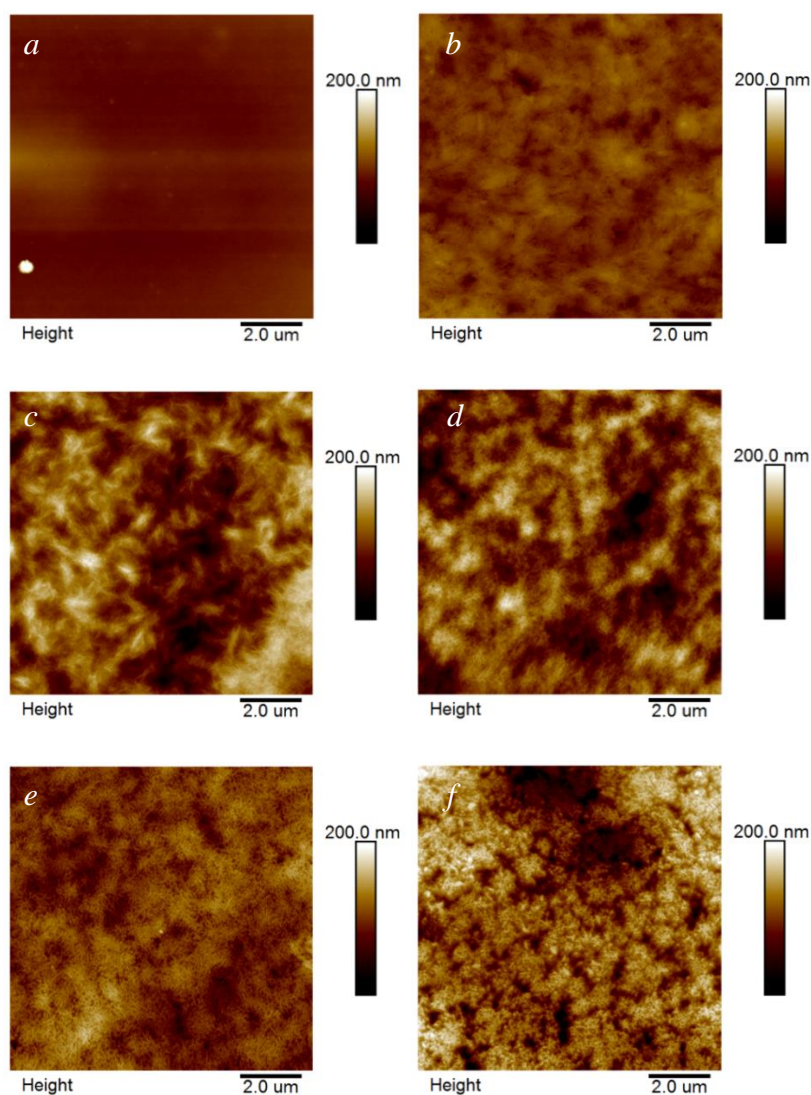


Figure 9. 10  $\mu\text{m}$  topography images of the surfaces of pure chitosan (*a*) and composites with 33 (*b*), 50 (*c*), 67 (*d*), 75 (*e*) and 82 (*f*) % of DES; resolution 768x256 pixels.

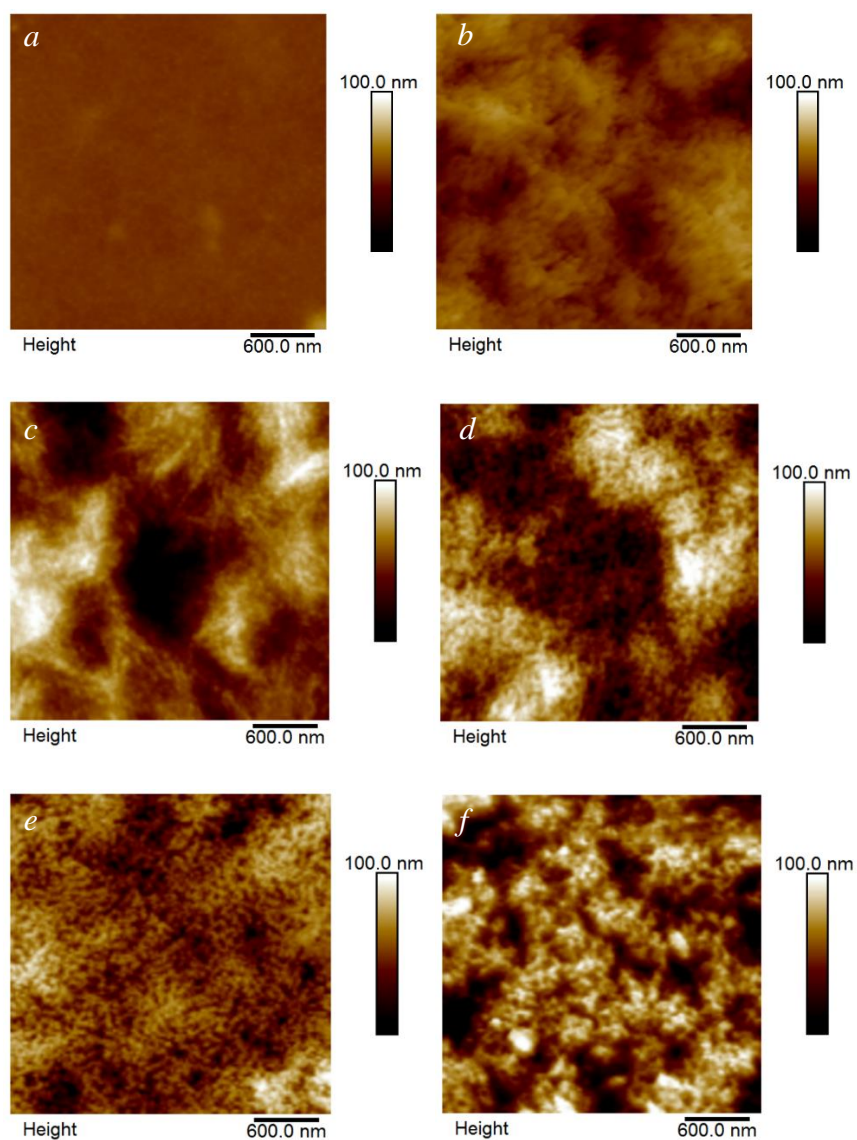


Figure 10. 3  $\mu\text{m}$  topography images of the surfaces of pure chitosan (*a*) and composites with 33 (*b*), 50 (*c*), 67 (*d*), 75 (*e*) and 82 (*f*) % of DES; resolution 128x128 pixels.

Table 5. Surface roughness

DES content, %	Rq, nm	
	10 $\mu\text{m}$ images	3 $\mu\text{m}$ images
0	8.35	1.75
33	11.2	8.96
50	29.3	19.8
67	27.7	21.3
75	17.9	14.3
82	32.4	20.7

## 6.2. Mechanical properties

Young's modulus values were calculated using the DMT model and Sneddon model (these values will be referred to as DMT modulus and Sneddon modulus). An example of the images obtained for the sample with 33% of DES is depicted in the Figure 11. Sneddon modulus was several orders of magnitude higher than DMT modulus, which was also the case for other samples. Taking into account the macroscopic data on samples stiffness, it was evident that Sneddon model failed to describe the interaction of the probe tip with these samples adequately. Thus, later in this work we used the DMT model.

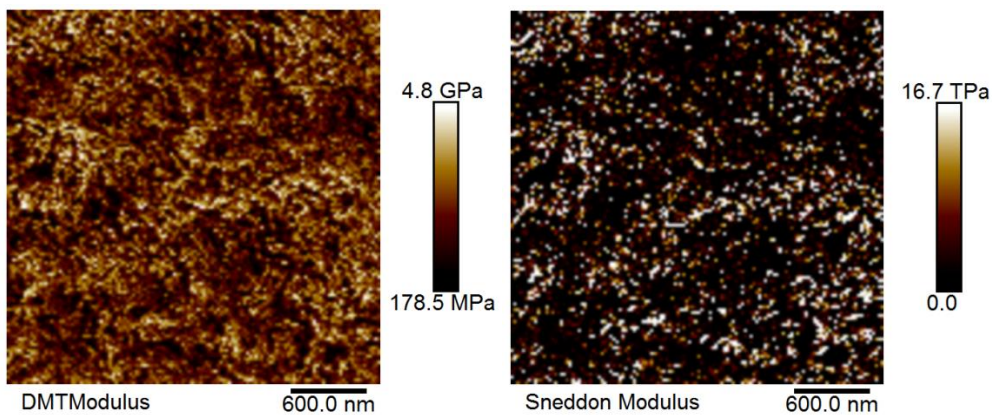


Figure 11. Young's modulus calculated using DMT (left) and Sneddon (right) models for the sample with 33% of DES.

The 3  $\mu\text{m}$  images (Figure 12) used for calculations of mean Young's modulus were taken with the resolution 128x128, i.e. for each pixel the modulus value was obtained from 26 force-separation curves. 10  $\mu\text{m}$  images were taken with higher resolution, but with less number of curves per pixel. The mean Young's modulus was found to decrease with DES content increase (Figure 13 *a*). This result was in good qualitative agreement with the macroscopic data; however, at DES content  $\geq 50\%$  Young's modulus measured via AFM was several times higher than Young's modulus calculated from the bulk measurements in the extension mode (Figure 13 *b*). This may be due to the differences in material properties on the surface and in the bulk, and these differences may be more significant for the samples with higher DES content.

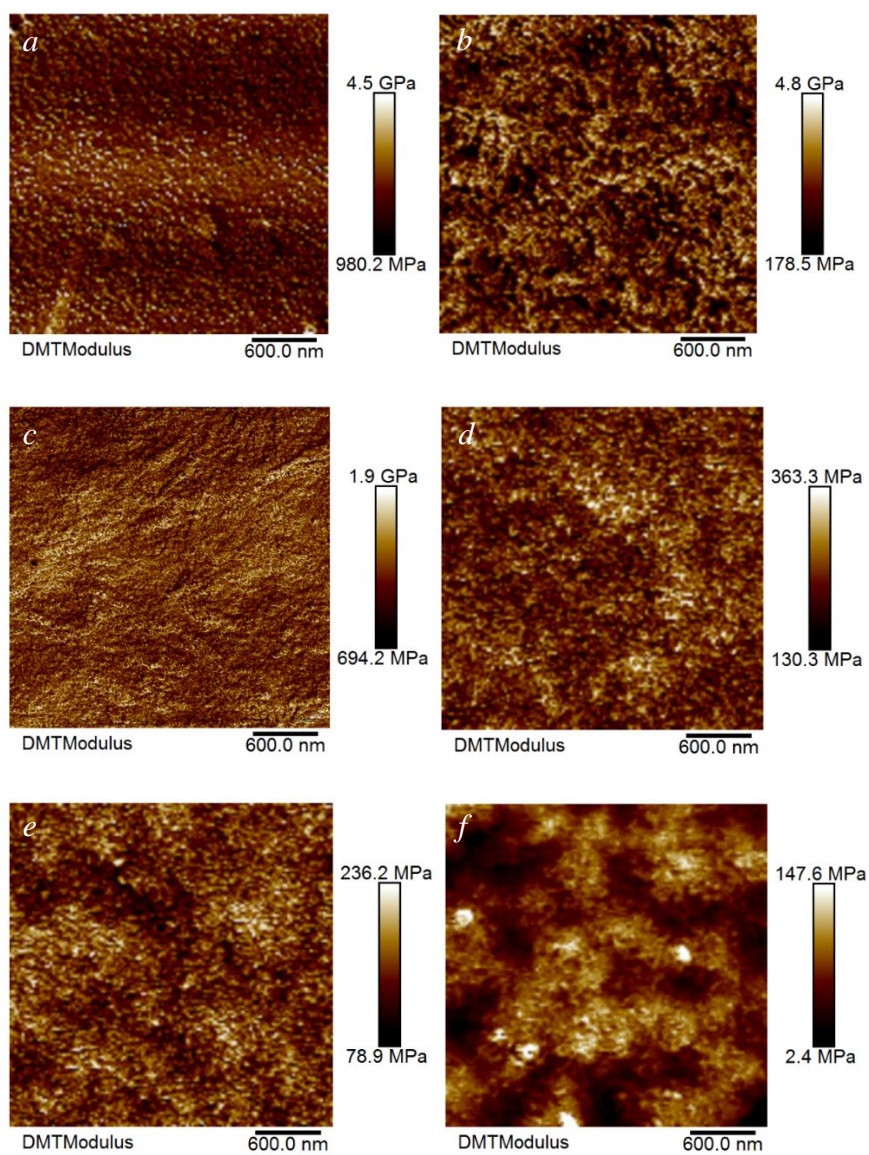


Figure 12. Maps of Young's modulus for pure chitosan (*a*) and composites with 33 (*b*), 50 (*c*), 67 (*d*), 75 (*e*) and 82 (*f*) % of DES.

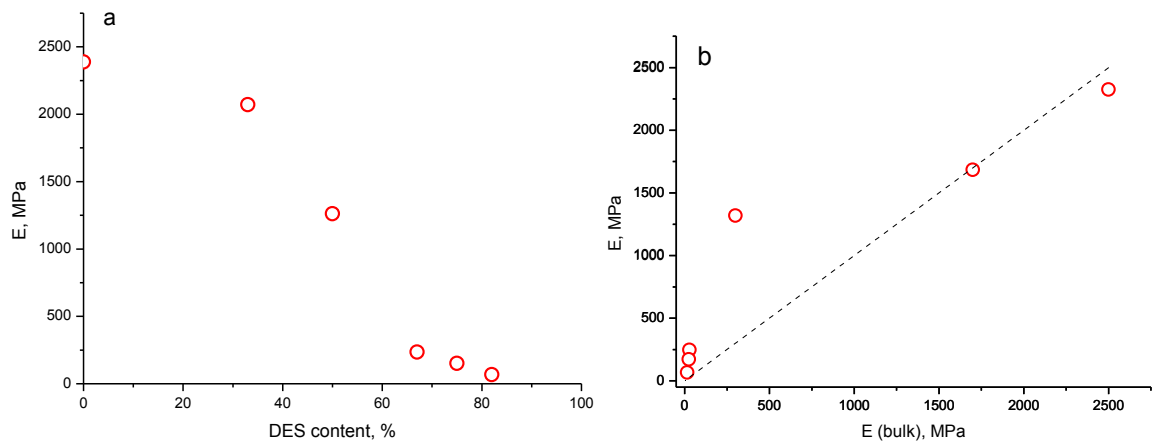


Figure 13. *a*) mean Young's modulus  $E$  dependence on the DES content, *b*) correlation between AFM results and results of bulk measurements in the extension mode,  $E$  and  $E$  (bulk), respectively (dashed line corresponds to equal values of  $E$  (bulk) and  $E$ ).

At the DES content of 82% the areas with different Young's modulus were distinguishable. Laying the DMT modulus color scale over the 3D topography image (Figure 14) shows that the lower modulus values correspond to the valleys, which may indicate the DES localization in these regions. However, applied force could be different in the valleys and at the hills, which could affect the registered Young's modulus. Since the probe was too stiff for this sample, the Young's modulus map could include artifacts. In order to make a more reliable conclusion, the measurements should be conducted with more appropriate probes.

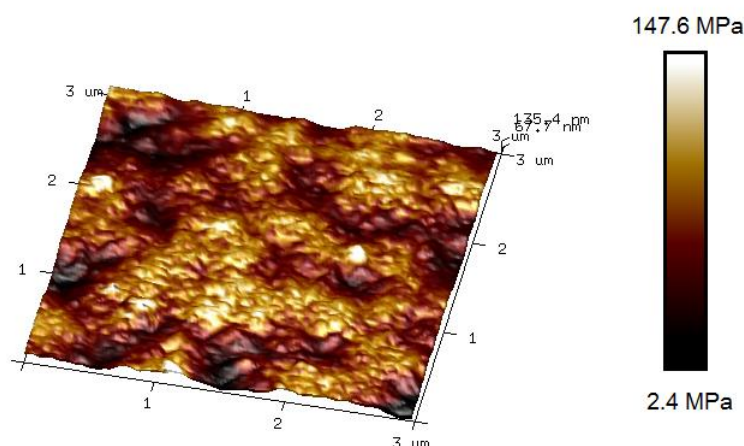


Figure 14. The overlaying of the DMT modulus color scale and the 3D topography for the sample with 82% of DES ( $x$ ,  $y$  and  $z$  axes are represented in real aspect ratio).

These regions are even more distinguishable on second, upper side of this sample (Figure 15). The adhesion is also different from the adhesion in neighboring areas. Thus, we can suppose that phase separation occurs in the sample with 82% of DES. Figure 12 *e* allows for an assumption that there are different phases also in the sample with 75% of DES.

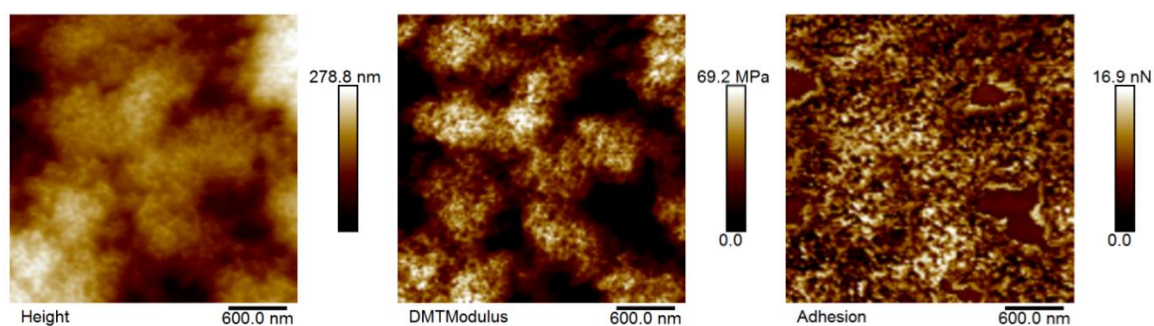


Figure 15. Topography, DMT modulus and adhesion images for the upper side of the sample with 82% of DES.

Since no clear correlation between DES content and adhesion values was found (Figure 16), it is not possible to determine the composition of different phases basing on the adhesion values.

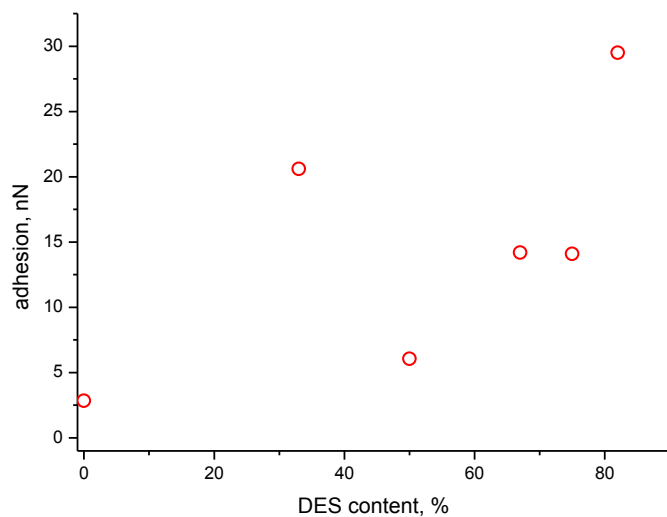


Figure 16. Adhesion dependence on the DES content.

### 6.3. Electrical properties

The conductivity measurements were carried out in the PF-TUNA mode using two different conductive probes: HA\_FM/W<sub>2</sub>C with label spring constant 3.5 N/m, and PtIr covered probe PF TUNA with label spring constant 0.4 N/m.

When the sample with DES content of 50% was studied with HA\_FM/W<sub>2</sub>C probe, the current did not exceed the noise level. Then the sample with the highest DES content (82%) was studied with the same probe, as it was expected to possess the highest conductivity among the samples. For this sample the signal of several tens of pA was observed under the voltage from -1.5 V to 1.0 V applied to the sample. During the measurements the sample was drifting, probably due to unsteady fixing. Topography and current maps for the sample with DES content of 82% under the applied voltages of -0.5 V and -1.0 V are represented in Figure 17. Under the positive voltage the sample was unstable; however, after returning to the negative voltage, it was again possible to observe the similar current maps. The areas with higher current were distinguishable mainly in the valleys, which may be the further evidence of DES localization in these areas.

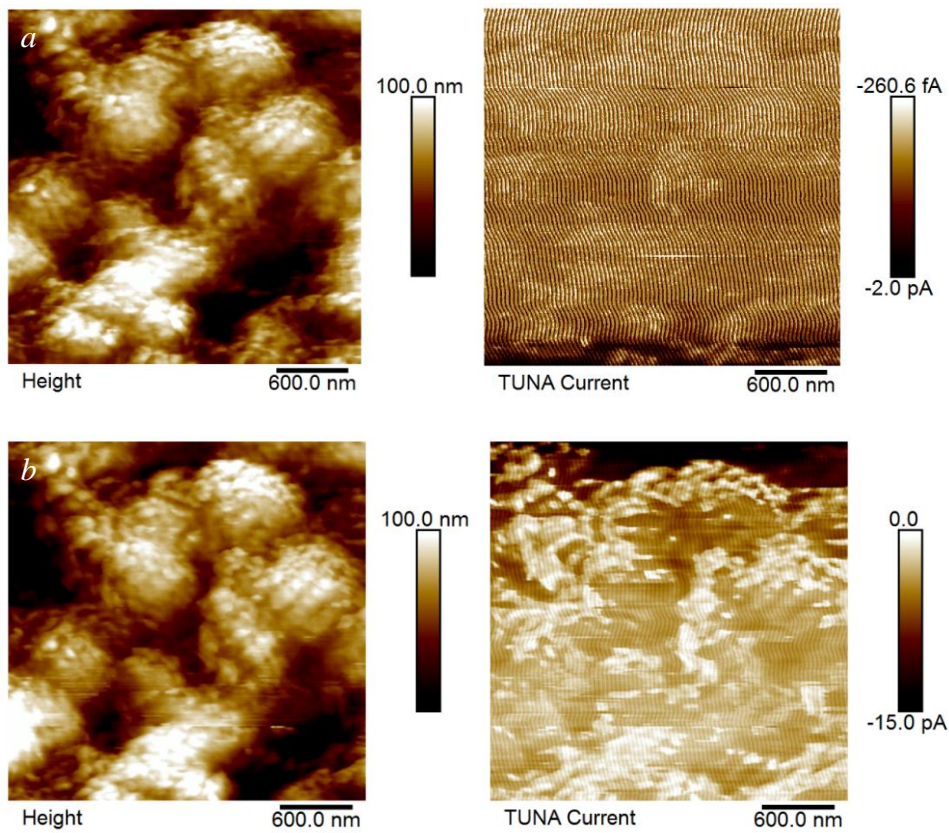


Figure 17. Topography (left) and current (right) maps at different voltage applied to the sample: -0.5 V (a) and -1.0 V (b).

I-V curves were recorded in different directions (starting from positive or from negative bias) at different ramp rates (Figure 18). The hysteretic behavior of I-V curves shows that the material exhibits capacitive properties of charge storage, and the bumps are attributed to the proceeding of the electrochemical reactions.

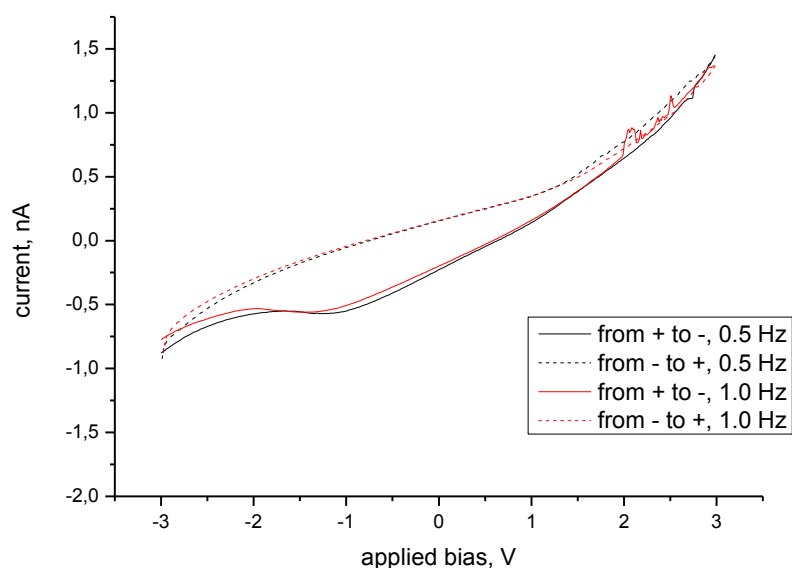


Figure 18. I-V curves, recorded in different directions (starting from positive or from negative bias) at different ramp rates.

Further measurements were conducted using PtIr covered probe as it was expected to accelerate the electrochemical reactions and to reduce their impact on the measured resistivity. The voltage range for PF-TUNA measurements was decreased to  $-0.5 \dots +0.5$  V.

For the sample with DES content of 67% the registered current did not exceed the noise level; however, the adhesion was found to be bias-dependent (figures 19–21). Under negative bias, surface heterogeneity was observed with presence of highly adhesive areas. Under a positive bias, the adhesion was lower and more homogeneous, and when bias was turned off, the adhesion map resembled that for the negative bias. Such behavior may be associated with migration of negatively charged constituents of DES to the anode. The morphology also changed slightly under the applied bias; under the positive bias the image was clearer.

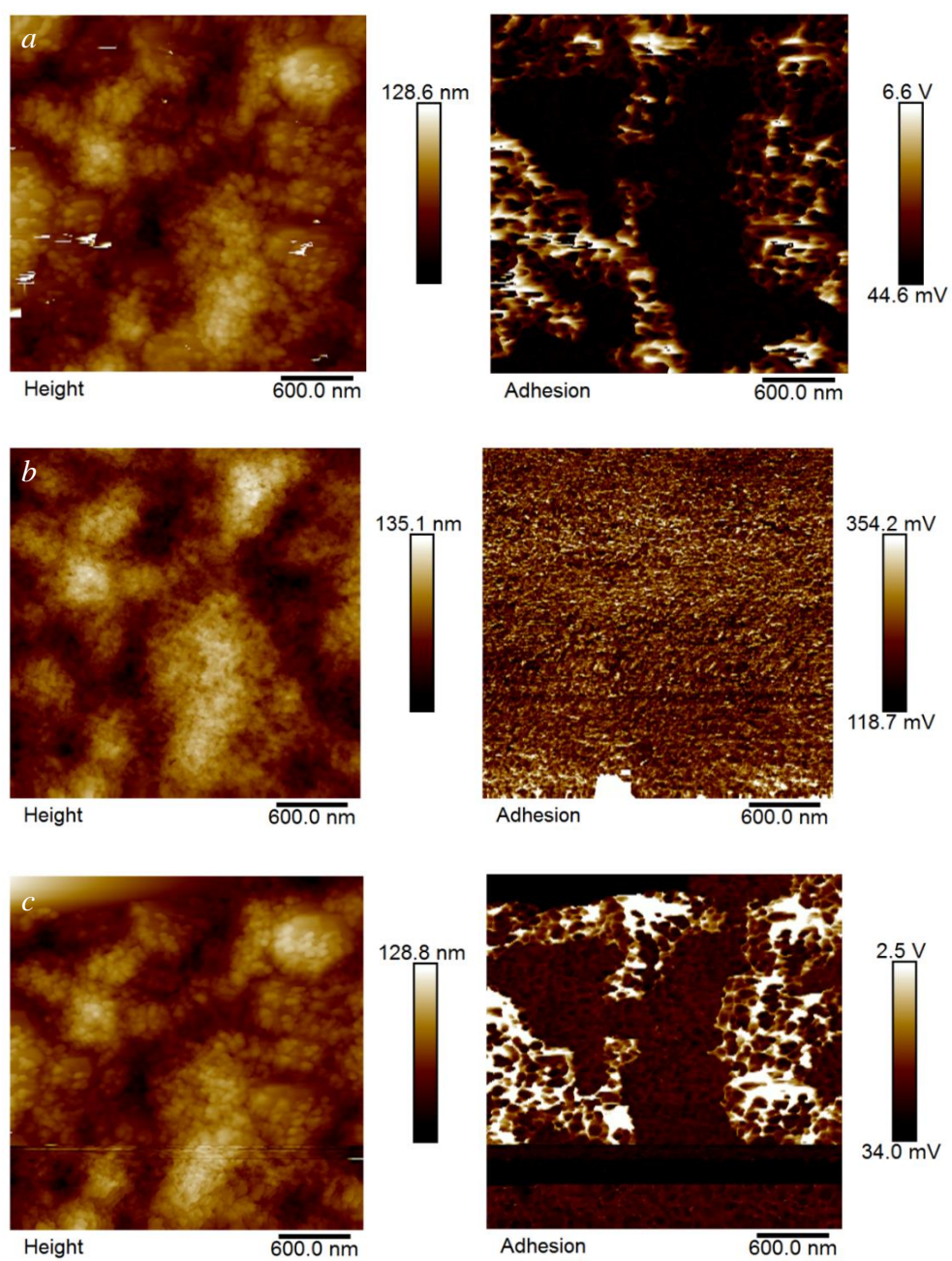


Figure 19. 3 μm topography (left) and adhesion (right) maps for the sample with DES content of 67% under different bias: -0.5V (a), +0.5V (b) and 0V (c).

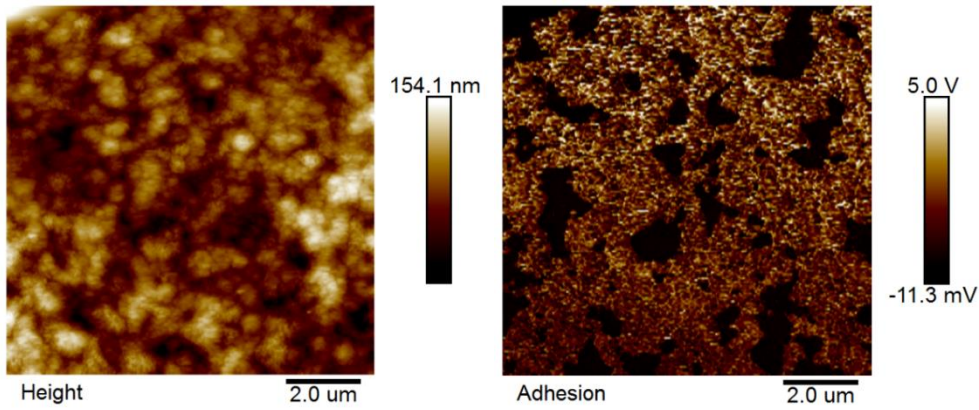


Figure 20. 10  $\mu\text{m}$  topography (left) and adhesion (right) maps for the sample with DES content of 67% under the applied bias of -0.5 V.

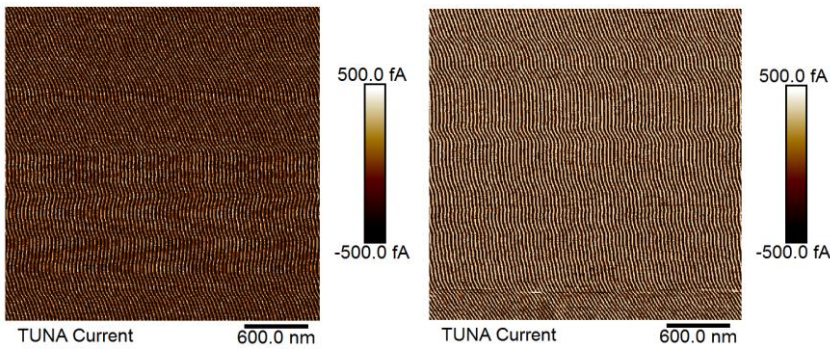


Figure 21. Current maps for the sample with DES content of 67% under the applied bias of -0.5 V (left) and +0.5 V (right)

Topography, adhesion and current maps for the sample with 75% of DES are represented in Figure 22. For the sample with DES content of 75% the adhesion was also found to be bias-dependent, and all the images were clearer under the positive bias. In addition, the fiber-like structures with low adhesion were clearly visible. The previous experiments did not reveal these structures that clearly, apparently because the probe used for the mechanical properties determination (42 N/m) was less suitable for soft samples than this probe (0.4 N/m). When the sample is positively biased, there was hardly distinguishable current in the region of these structures.

I-V curves for the sample with DES content of 75% (Figure 23) exhibited hysteretic behavior similar to I-V curves for the sample with DES content of 67%.

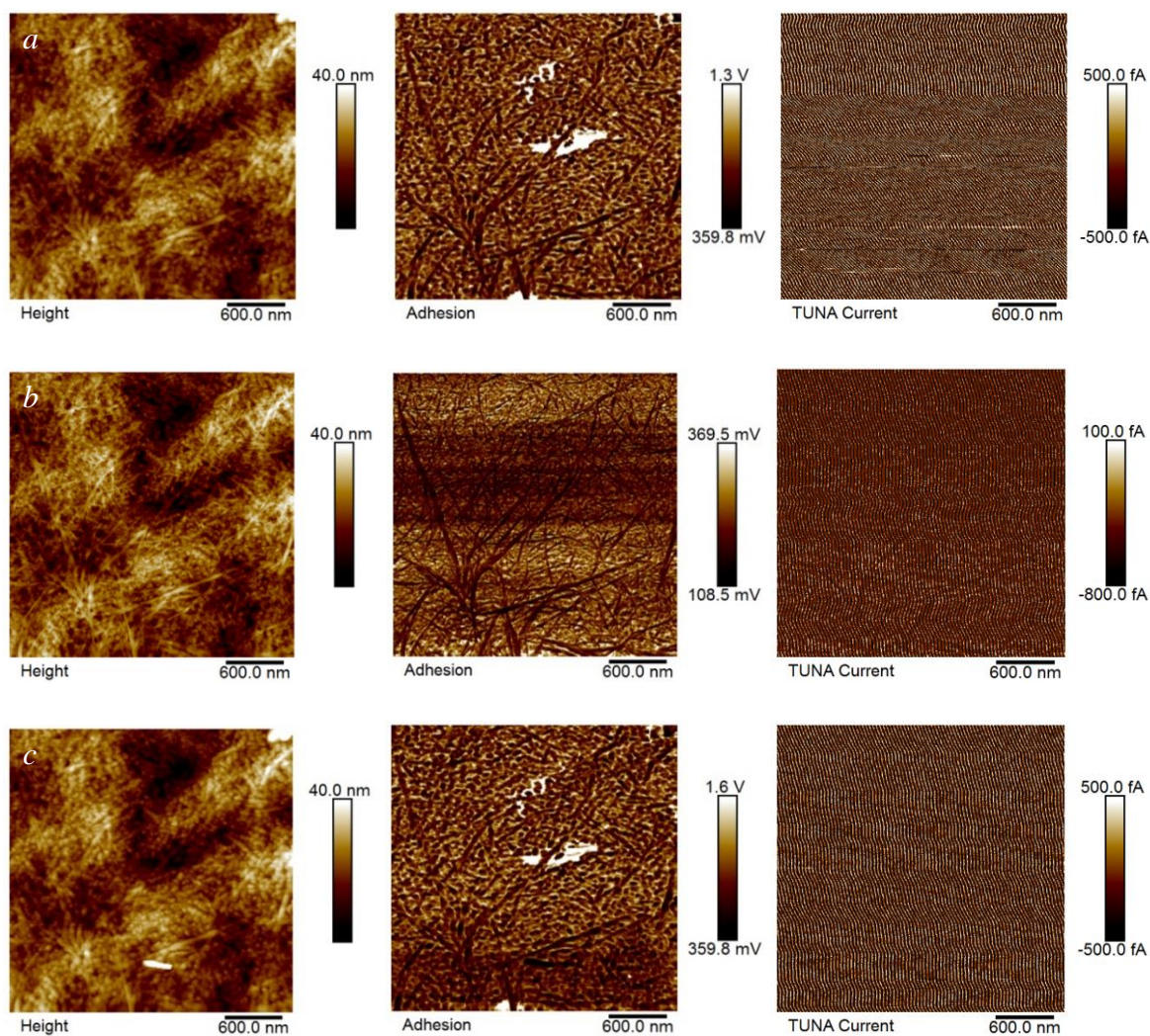


Figure 22. 3  $\mu\text{m}$  images of topography (left), adhesion (center) and TUNA current (right) for the sample with DES content of 75% under different bias: -0.5V (a), +0.5V (b) and 0V (c).

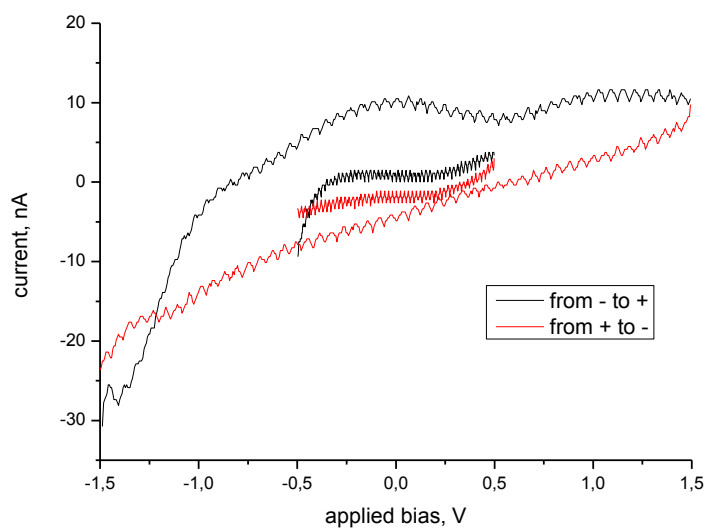


Figure 23. I-V curves for the sample with DES content of 75%.

The images obtained for the sample with DES content of 75% using HA\_FM/W<sub>2</sub>C probe were less clear, which can be due to the higher spring constant of this probe, and the current did not exceed the noise level.

## Conclusions

- 1) A set of composite membranes based on chitosan and DES was successfully prepared, including the films with high content of DES (up to 82%).
- 2) The AFM measurements of Young's modulus and adhesion showed that noticeable phase separation takes place in the sample containing 82% of DES. The phase separation can also be supposed for the sample with 75% DES. There was no evidence of phase separation for other samples.
- 3) Topography maps showed that integration of DES into the chitosan matrix led to the formation of anisotropic objects on the film surface with sizes about 50 nm, while the surface of pure chitosan was smooth.
- 4) The AFM measurements of Young's modulus revealed that increase of DES content led to the decrease of the composite stiffness. This result is in qualitative agreement with bulk measurements of mechanical modulus by uniaxial extension. However, at DES content  $\geq 50\%$  Young's modulus values obtained by AFM method were several times higher than calculated from bulk measurements. This may be due to the differences in material properties on the surface and in the bulk.
- 5) In order to investigate the conductivity of the material at nanoscale, the maps of current through the film surface were obtained. Measurable currents in scanning mode were observed only in the case of sample with 82% of DES. Topography and adhesion of the composite films surface was shown to depend on the polarity of applied electrical potential: the observable surface features grew in size and adhesion increased under the negative bias.

## Summary

In this work the newly synthesized composite films based on chitosan and deep eutectic solvent (DES), namely a eutectic mixture of choline chloride and malonic acid, were studied by means of AFM. Measurements were conducted using Bruker Multimode 8 AFM and “Nanoscope” software package. Two operational modes of AFM were used for measurements: PeakForce QNM and PeakForce TUNA. These modes allow for simultaneous mapping of topography, mechanical properties and, in the case of PF-TUNA, electrical properties.

The main highlights of this work are as follows:

- 1) Phase separation was observed for sample with 82% of DES and was supposed to take place also for sample with 75% of DES;
- 2) The Young’s modulus decreased with the DES content increase, which was in qualitative agreement with bulk measurements;
- 3) Measurable currents in scanning mode were observed only for sample with 82% of DES; however, the topography and adhesion of samples with high DES content was shown to be bias-dependent.

It is necessary to know the mechanical properties of the material in order to understand possibilities and limitations for its applications. The micro-scale response to the electric field is important for potential application of the studied composites as artificial muscles.

This research can be further improved, if the appropriate probes are selected individually for each sample considering the preliminary data on the stiffness. This may give more precise values of Young’s modulus and adhesion as well as topography and mechanical properties maps of higher resolution. Electrical measurements have room for improvement; in particular, if the sample with highest DES content (82%) is measured with PF-TUNA probe, as it was done for two other samples, more informative maps of current may be obtained.

This work gives also several ideas for more extensive research, which would have the practical relevance.

Firstly, since the bias applied to the composite membrane causes the morphology changes, these systems can probably act as artificial muscles. Therefore, it would be of use to measure their electromechanical response.

Secondly, in order to study properties in the bulk, the samples could be fractured in liquid nitrogen and the cross section could be studied by means of AFM (at temperatures lower than glass transition temperature of the composite film).

Finally, taking into account the reported application of DESs for liquid separation, it would be reasonable to study the liquid separation properties of these composite membranes.

## References

1. Gal'braikh, L.S. 2001. Hitin i hitozan: stroenie, svoistva, primenenie. *Sorosovskii obrazovatel'nyi zhurnal*, №1 pp. 51–56. (in Russian)
2. Dutta, P.K., Dutta, J., Tripathi, V.S. 2004. Chitin and chitosan: Chemistry, properties and applications. *Journal of Scientific & Industrial Research*, vol. 63, pp. 20–31.
3. Maksimov, I.V. 2013. Biological activity of chitin and sphere of its application. *Proceedings of the RAS Ufa Scientific Centre*, №2, pp. 38–61. (in Russian)
4. Earle, M.J. & Seddon, K.R. 2000. Ionic liquids. Green solvents for the future. *Pure Appl. Chem.* 72, pp. 1391–1398.
5. Petkovic, M., Seddon, K.R., Rebelo, L.P., Silva Pereira, C. 2011. Ionic liquids: a pathway to environmental acceptability. *Chem. Soc. Rev.* 40, pp. 1383–1403.
6. Ghandi K. 2014. A Review of Ionic Liquids, Their Limits and Applications. *Green and Sustainable Chemistry*, 4, pp. 44-53.
7. Plechkova, N.V. & Seddon, K.R. 2007. Applications of ionic liquids in the chemical industry. *Chem. Soc. Rev.*, vol. 37, pp. 123–150.
8. Abbott, A.P., Boothby, D., Capper, G., Davies, D.L., Rasheed, R.K. 2004. Deep Eutectic Solvents Formed between Choline Chloride and Carboxylic Acids: Versatile Alternatives to Ionic Liquids. *J. Am. Chem. Soc.*, vol. 126, pp. 9142–9147.
9. Zhao, H. & Baker G.A. 2013. Ionic liquids and deep eutectic solvents for biodiesel synthesis: a review. *J. Chem. Technol. Biotechnol.*, vol. 88, pp. 3–12.
10. Wang, F., Jeon, J., Park, S., Kee, Ch., Kimc, S., Oh, I. 2016. Soft biomolecule actuator based on highly functionalized bacterial cellulose nano-fiber network with carboxylic acid groups. *Soft Matter*, vol. 12, 246–254.
11. Scovazzo, P., Kieft, J., Finan, D.A., Koval, C., DuBois, D., Noble, R. 2004. Gas separations using non-hexafluorophosphate [PF<sub>6</sub>](<sup>-</sup>) anion supported ionic liquid membranes. *J. Membr. Sci.*, 238, pp. 57–63.

13. Park, Y., Kim, B., Byun, Y., Lee, S., Lee, E., Lee, J. 2009. Preparation of supported ionic liquid membranes (SILMs) for the removal of acidic gases from crude natural gas. *Desalination*, 236, pp. 342–348.
12. Scovazzo, P., Visser, A., Davis, J., Rogers, R., Koval, C., DuBois, D., Noble, R. Supported ionic liquid membranes and facilitated ionic liquid membranes (FILMs) (In: *Industrial Applications of Ionic Liquids*. Ed. Rogers, R., Seddon, K. American Chemical Society Books, 2002, Chapter 6).
14. Jiang, Y., Zhou, Z., Jiao, Z., Li, L., Wu, Y., Zhang, Z. 2007. SO<sub>2</sub> gas separation using supported ionic liquid membranes. *J. Phys. Chem*, B111, pp. 5058–5061.
15. Lianga, L., Ganb, Q., Nancarrow, P. 2014. Composite ionic liquid and polymer membranes for gas separation at elevated temperatures. *Journal of Membrane Science*, vol. 450, pp. 407–417.
16. Rdzanek, P., Heitmann, S., Górak, A., Kaminski, W. 2015. Application of supported ionic liquid membranes (SILMs) for biobutanol pervaporation. *Separation and Purification Technology*, vol. 155, pp. 83–88.
17. Heitmann, S., Krings, J., Kreis, P., Lennert, A., Pitner, W.R., Górak, A., Schulte, M.M. 2012. Recovery of n-butanol using ionic liquid-based pervaporation membranes. *Separation and Purification Technology*, vol. 97, 108–114.
18. Wang, F., Jeon, J., Kim, S., Park, J., Park, S. 2016. An eco-friendly ultra-high performance ionic artificial muscle based on poly (2-acrylamido-2-methyl-1-propanesulfonic acid) and carboxylate bacterial cellulose. *J. Mater. Chem. B*, vol. 4, pp. 5015–5024.
19. Li, J., Wilmsmeyer, K.G., Hou, J., Madsen, L.A. 2009. The role of water in transport of ionic liquids in polymeric artificial muscle actuators. *Soft Matter*, vol. 5, pp. 2596–2602.
20. Okazaki, H., Sawada, Sh., Matsuda, T., Kimura, M. 2014. Soft Actuator using Ionic Polymer-Metal Composite driven with Ionic Liquid. IEEE International Meeting for Future of Electron Devices, Kansai (IMFEDK), 19–20 June, Kansai, Japan.

21. Bubalo, M.C., Radošević, K., Redovniković, I.R., Halambek, J., Srček, V.G. 2014. A brief overview of the potential environmental hazards of ionic liquids. *Ecotoxicology and Environmental Safety*, vol. 99, pp. 1–12.
22. Abbott, A.P., Capper, G., Davies, D.L., Munro, H.L., Rasheed, R.K., Tambyrajah, V. 2001. Preparation of novel, moisture-stable, Lewis-acidic ionic liquids containing quaternary ammonium salts with functional side chains. *Chem. Commun.*, vol. 19, pp. 2010–2011
23. Abbott, A.P., Capper, G., Davies, D.L., Rasheed, R.K., Tambyrajah, V. 2003. Novel solvent properties of choline chloride/urea mixtures. *Chem. Commun.*, vol. 1, pp. 70–71.
24. Zhang, Q., De Oliveira Vigier, K., Royer, S., Jérôme, F. 2012. Deep eutectic solvents: syntheses, properties and applications. *Chem. Soc. Rev.*, vol. 41, pp. 7108–7146.
25. Smith, E.L., Abbott, A.P., Ryder, K.S. 2014. Deep Eutectic Solvents (DESs) and Their Applications. *Chem. Rev.*, vol. 114, pp. 11060–11082.
26. Abbott, A.P., Ballantyne, A.D., Conde, J.P., Ryder, K.S., Wise, R.W. 2012. Salt modified starch: sustainable, recyclable plastics. *Green Chem.*, vol. 14, pp. 1302–1307.
27. Leroy, E., Decaen, P., Jacquet, P., Coativy, G., Pontoire, B., Reguerre, A., Lourdin, D. 2012. Deep eutectic solvents as functional additives for starch based plastics. *Green Chem.*, vol. 14, pp. 3063–3066.
28. Abbott, A.P., Abolibda, T.Z., Qu, W., Wise, W.R., Wright, L.A. 2017. Thermoplastic starch–polyethylene blends homogenised using deep eutectic solvents. *RSC Adv.*, vol. 7, pp. 7268–7273.
29. Shamsuri, A.A. & Daik, R. 2012. Plasticizing effect of choline chloride/urea eutectic-based ionic liquid on physicochemical properties of agarose films. *BioResources*, vol. 7(4), pp. 4760–4775.
30. Sousa, A.M.M., Souza, H.K.S., Latona, N., Liu, Ch., Gonçalves, M.P., Liu, L. 2014. Choline chloride based ionic liquid analogues as tool for the fabrication of agar films with improved mechanical properties. *Carbohydrate Polymers*, vol. 111, pp. 206–214.

31. Galvis-Sánchez, A.C., Sousa, A.M.M., Hilliou, L., Gonçalves, M.P., Souza, H.K.S. 2014. Thermo-compression molding of chitosan with a deep eutectic mixture for biofilms development. *Green Chem.*, vol. 18, pp. 1571–1580.
32. Smolyakov, G, Pruvost, S, Cardoso, L, Alonso, B, Belamie, E, Duchet-Rumeau, J. 2016. AFM PeakForce QNM mode: Evidencing nanometre-scale mechanical properties of chitin-silica hybrid nanocomposite. *Carbohydrate Polymers*, vol. 151, pp. 373–380.
33. Hiesgen, R., Helmly, S., Galm, I., Morawietz, T., Handl, M., Friedrich, K.A. 2012. Microscopic Analysis of Current and Mechanical Properties of Nafion® Studied by Atomic Force Microscopy. *Membranes*, vol. 2(4), pp. 783-803
34. Sokolova, M.P., Smirnov, M.A., Geydt, P., Bugrov, A.N., Ovaska S., Lahderanta E., Toikka, A.M. 2016. Structure and Transport Properties of Mixed-Matrix Membranes Based on Polyimides with ZrO<sub>2</sub> Nanostars. *Polymers*, vol. 8, p. 403.
35. Application Note #141 Toward Quantitative Nanomechanical Measurements on Live Cells with PeakForce QNM 2013 Bruker Corporation.
36. Application Note #128 Quantitative Mechanical Property Mapping at the Nanoscale with PeakForce QNM 2010 Bruker Corporation.
37. Application Note #132 Simultaneous Electrical and Mechanical Property Mapping at the Nanoscale with PeakForce TUNA 2011 Bruker Corporation.
38. Bykova, V.M., Nemtsev, S.V. Syr'evye istochniki I sposoby polucheniya hitina I hitozana (In: Chitin and Chitosan: Production, Properties and Usage. Ed. Skryabin, K.G., Vikhoreva, G.A., Varlamov, V.P. Moscow: Nauka, 2002, pp. 7–23). (in Russian)
39. Nud'ga, L.A. Proizvodnye hitina i hitozana i ih svoistva (In: Chitin and Chitosan: Production, Properties and Usage. Ed. Skryabin, K.G., Vikhoreva, G.A., Varlamov, V.P. Moscow: Nauka, 2002, pp. 141–177). (in Russian)
40. Gorovoi, L.F., Kosyakov, V.N. Sorbtsionnye svoistva hitina i ego proizvodnyh (In: Chitin and Chitosan: Production, Properties and Usage. Ed. Skryabin, K.G., Vikhoreva, G.A., Varlamov, V.P. Moscow: Nauka, 2002, pp. 217–246). (in Russian)

41. Safronova, T.M. Primenenie hitozana v proizvodstve pischevykh produktov (In: Chitin and Chitosan: Production, Properties and Usage. Ed. Skryabin, K.G., Vikhoreva, G.A., Varlamov, V.P. Moscow: Nauka, 2002, pp. 346–359). (in Russian)
42. Albulov, A.I., Samuilenko, A.Ya., Frolova, M.A. Hitozan v kosmetike. (In: Chitin and Chitosan: Production, Properties and Usage. Ed. Skryabin, K.G., Vikhoreva, G.A., Varlamov, V.P. Moscow: Nauka, 2002, pp. 360–363). (in Russian)
43. Lopatin, S.A. Hitozan v hromatografii (In: Chitin and Chitosan: Production, Properties and Usage. Ed. Skryabin, K.G., Vikhoreva, G.A., Varlamov, V.P. Moscow: Nauka, 2002, pp. 247–253). (in Russian)
44. Koev, S.T., Dykstra, P.H., Luo, X., Rubloff, G.W., Bentley, W.E., Payne, G.F., Ghodssi, R. 2010. Chitosan: an integrative biomaterial for lab-on-a-chip devices. *Lab Chip*, vol.10, pp. 3026–3042.
45. Markvicheva, E.A. Hitozan i ego proizvodnye v biokapsulirovanii (In: Chitin and Chitosan: Production, Properties and Usage. Ed. Skryabin, K.G., Vikhoreva, G.A., Varlamov, V.P. Moscow: Nauka, 2002, pp. 315–326). (in Russian)
46. Bol'shakov, I.N., Nasibov, S.M., Kuklin, E.Yu., Prihod'ko, A.A. Ispol'zovanie hitozana i ego produktov pri vospalitel'nykh zabolevaniyakh zheludochno-kishechnogo trakta (In: Chitin and Chitosan: Production, Properties and Usage. Ed. Skryabin, K.G., Vikhoreva, G.A., Varlamov, V.P. Moscow: Nauka, 2002, pp. 280–301). (in Russian)
47. Drozd, N.N., Makarov, V.A. Antikoagulyantnaya aktivnost' sul'fatirovannykh proizvodnykh hitozana (In: Chitin and Chitosan: Production, Properties and Usage. Ed. Skryabin, K.G., Vikhoreva, G.A., Varlamov, V.P. Moscow: Nauka, 2002, pp. 302–314). (in Russian)
48. Zhogolev, K.D., Nikitin, V.Yu., Tsygan, V.N. 2003. Hitozan — perspektivy primeneniya v medicine. *Journal of new medical technologies*, vol.10, №1-2, pp. 94–96. (in Russian)
49. Boyarintsev, V.V., Fronchek, E.V., Trofimenko, A.V., Fil'kov, G.I. 2014. Sredstvo perevyazochnoe gemostaticheskoe “Gemohit®” — innovatsionnye biotekhnologii v ekstremal'noi meditsine. Proceedings of 12th International Conference “Modern

perspectives in studies of chitin and chitosan” (Roshit2014), RAS Center “Bioengineering”, Moscow, Russia, pp. 64–66. (in Russian)

50. Andranovich, S., Golyshev, A.A., Voronina, N.G., Steinhoff, G., Skorik, Yu.A. 2014. Genno-terapevticheskie vektory na osnove hitozana. Proceedings of 12 International Conference “Modern perspectives in studies of chitin and chitosan” (Roshit2014), RAS Center “Bioengineering”, Moscow, Russia, pp. 22–27. (in Russian)

51. Panarin, E.F., Nud’ga, L.A., Petrova, V.A., Bochek, A.M., Gofman, I.V., Baklagina, Yu.G., Blinova, M.I., Spichkina, O.P., Yudintseva, N.M., Pinaev, G.P. 2009. Matritsy dlya kul’tivirovaniya kletok kozhi cheloveka na osnove prirodnyh polisaharidov — hitina i hitozana. *Geny i kletki*, vol.4, №3, pp. 42–46. (in Russian)

52. Francisco, M., van den Bruinhorsta, A., Zubeira, L.F., Peters, C.J., Kroon, M.C. 2013. A new low transition temperature mixture (LTTM) formed by choline chloride + lactic acid: Characterization as solvent for CO<sub>2</sub> capture. *Fluid Phase Equilibria*, vol. 340, pp. 77–84.

53. Paiva, A., Craveiro, R., Aroso, I., Martins, M., Reis, R.L., Duarte, A.R.C. 2014. Natural Deep Eutectic Solvents – Solvents for the 21st Century. *ACS Sustainable Chem. Eng.*, vol. 2, pp. 1063–1071

54. Abo-Hamad, A., Hayyan, M, AlSaadi, M.A., Hashim, M.A. 2015. Potential applications of deep eutectic solvents in nanotechnology. *Chemical Engineering Journal*, vol. 273, pp. 551–567.

55. Abbott, A.P., Capper, G., Gray, S. 2006. Design of improved deep eutectic solvents using hole theory. *Chem. Phys. Chem.*, vol. 7, pp. 803–806.

56. García, G., Aparicio, S., Ullah, R., Atilhan, M. 2015. Deep Eutectic Solvents: Physicochemical Properties and Gas Separation Applications. *Energy Fuels*, vol. 29, pp. 2616–2644.

57. Francisco, M., van den Bruinhorsta, A., Kroon, M.C. 2015. Low-Transition-Temperature Mixtures (LTTMs): A New Generation of Designer Solvents. *Angew. Chem. Int. Ed.*, vol. 52, pp. 3074–3085.

58. Oliveira, F.S., Pereiro, A.B., Rebelo, L.P.N., Marrucho, I.M. 2013. Deep eutectic solvents as extraction media for azeotropic mixtures. *Green Chem.*, vol. 15, pp. 1326–1330.
59. Colomines, G., Decaen, P., Lourdin, D., Leroy, E. 2016. Biofriendly ionic liquids for starch plasticization: a screening approach. *RSC Adv.*, vol. 6, pp. 90331–90337.
60. V. Mironov. 2004. Fundamentals of Scanning Probe Microscopy, N.Novgorod (in Russian).
61. Schönherr, H. & Julius Vancso, G.J. 2010. Atomic Force Microscopy in Practice, Scanning Force Microscopy of Polymers, Springer Laboratory.
62. Bruker AFM probes. [accessed 30.04.2017] Available at <http://www.brukerafmprobes.com>
63. ScanSens GmbH. [accessed 30.04.2017] Available at <http://www.scansens.com>
64. D. Maugis, Contact, Adhesion and Rupture of Elastic Solids (Springer-Verlag, Berlin, 2000)